The Dissertation Committee for Vera Sue Myers Certifies that this is the approved version of the following dissertation:

Characterization of Dendrimer Encapsulated Nanoparticles by Extended X-ray Absorption Fine Structure and Electrochemical Methods

Committee:

Richard Crooks, Supervisor

Graeme Henkelman

Keith Stevenson

Katherine Willets

Arumugam Manthiram

Anatoly Frenkel

Characterization of Dendrimer Encapsulated Nanoparticles by Extended X-ray Absorption Fine Structure and Electrochemical Methods

by

Vera Sue Myers, B.A.

Dissertation

Presented to the Faculty of the Graduate School of

The University of Texas at Austin

in Partial Fulfillment

of the Requirements

for the Degree of

Doctor of Philosophy

The University of Texas at Austin

December 2011

Dedication

To my husband, Jason.

Acknowledgements

I would like to thank my advisor, Prof. Richard Crooks, for the lessons he has taught me and for all his invaluable advice.

Many thanks go to my committee members, Prof. Arumugam Manthiram, Prof. Keith Stevenson, and Prof. Katherine Willets. I would also like to thank Prof. Graeme Henkelman for the many interesting collaborative meetings. The discussions held in these always renewed my excitement and enthusiasm for pursuing DENs research. I also greatly appreciate all of the patience and time Prof. Anatoly Frenkel afforded me. He is a great teacher and it was a pleasure to work with him.

For their assistance and support in the many stages of my research, I would like to thank Prof. Javier Guerra, Dr. Ioana Dumnitrescu, Dr. Mike Weir, Dr. Rachel Behrens, Stephen Fosdick, and Daphne Sung. Finally, I also thank my husband, Jason. Without him, none of this would have been possible.

Characterization of Dendrimer Encapsulated Nanoparticles by Extended X-ray Absorption Fine Structure and Electrochemical Methods

Vera Sue Myers, Ph.D.

The University of Texas at Austin, 2011

Supervisor: Richard M. Crooks

The small size regime and bulky hydrocarbon exterior of dendrimer encapsulated nanoparticles (DENs) often make characterization of these materials a unique challenge. Here, I report on three studies utilizing the techniques of extended X-ray absorption fine structure (EXAFS) and electrochemistry to probe the properties and behavior of these materials.

First, the synthesis and characterization of PdCu bimetallic nanoparticles, and Pd and Cu monometallic nanoparticles, consisting of an average of ~64 atoms is described. The bimetallic nanoparticles were prepared by co-complexation of Pd^{2+} and Cu^{2+} salts to interior functional groups of a dendrimer template followed by chemical reduction to yield DENs. EXAFS spectroscopy indicates that these particles have an alloy structure. This is a rare example of a stable nanoparticle in this size range that

consists of one reactive metal and one substantially more noble metal.

Second, in-situ electrochemical EXAFS is used to evaluate the structure of Pt DENs during the oxygen reduction reaction (ORR). The DENs contained an average of just 225 atoms each. The results indicate that the Pt coordination number (CN) decreases when the electrode potential is moved to positive values. The results are interpreted in terms of an ordered core, disordered shell model. The structure of the DENs is not significantly impacted by the presence of dioxygen, but other electrogenerated species may have a significant impact on nanoparticle structure.

Third, the electrochemical dissolution of Cu DENs is investigated using anodic stripping voltammetry (ASV). The effect of the scan rate and Cu loading on the electrode to the stripping wave is performed. The results indicate a large, positive shift of the stripping potential for the dendrimer-metal composites, but no size-dependent changes to peak position.

Table of Contents

Chapter 1: Introduction

1.1 Dendrimer Encapsulated Nanoparticles

Since it was first introduced in 1998,[1] the technique of dendrimer templating has proven to be a versatile method for synthesizing nanoparticles having well-defined sizes, compositions, and structures. The basic approach for synthesizing dendrimer-encapsulated nanoparticles (DENs) is comprised of two steps (Illustration 1.1).

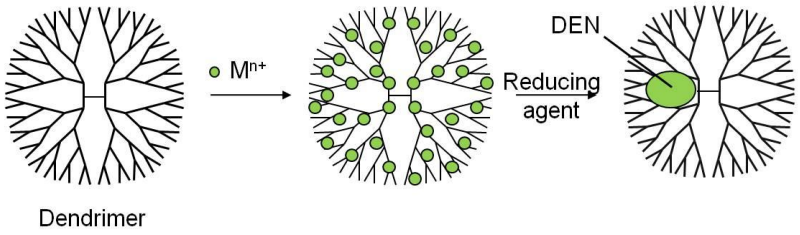

Illustration 1.1

First, appropriate metal ions are mixed with a dendrimer solution. This results in encapsulation of the metal ions within the dendrimer. The means by which metal ions complex to the dendrimer interior depends on the identity of the metal, and this effect has been investigated in several theoretical[2-5] and empirical[6-9] studies. Second, a chemical reducing agent is added to this solution resulting in the formation of DENs.

The DEN synthesis offers some significant advantages over other methods for preparing nanoparticles in the 1-2 nm

size range. Most of these advantages arise from the presence of the dendrimer, which both templates and stabilizes the encapsulated nanoparticles. For example, the composition of DENs can be selected by choosing the identity and ratio of metal ions complexed to the dendrimer in the first step of the synthesis. Likewise, the structure of DENs can also be controlled via slight variations to the synthetic procedure: simultaneous complexation and reduction of Pt^{2+} and Pd^{2+} ions within a sixth-generation, hydroxyl-terminated poly(amido amine) (PAMAM) dendrimer (G6-OH) results in bimetallic PtPd alloy nanoparticles.[10,11] In contrast, when the component metal ions are complexed and reduced sequentially, core@shell DENs may result.[12] The size of DENs is controlled by selecting the metal-ion: dendrimer ratio. DENs as large as 4 nm in diameter have been reported,[13] but the more typical size range is 1 to 2 nm.[14-17] The very small size of DENs is one of their main virtues, because the physical and chemical properties of metals change quickly in this size regime.[18,19]

In addition to their templating function, which largely controls the size, composition, and structure of DENs, the dendrimer also stabilizes the encapsulated nanoparticles against agglomeration. The nature of the dendrimer as a stabilizing agent is fundamentally different from other stabilizers, such as capping agents, because the dendrimer does not passivate or specifically coordinate to the

nanoparticle surface. In the case of DENs, the nanoparticles are sterically confined to the interior region of the dendrimer,[13] and the degree of chemical interaction of the dendrimer with the surface of the nanoparticle is minimal.[20,21] Accordingly, the surface of DENs is free to engage in catalytic reactions, as long as the substrate is small enough to penetrate the branched periphery of the dendrimer. Most other approaches for stabilizing nanoparticles rely on a specific chemical interaction between a ligand and the nanoparticle surface. Typically, this results in reduced access of reactants to surface atoms and, hence, lower reaction rates.[22-24]

Another advantage of the dendrimer is that its periphery consists of many tens, or even thousands, of individual functional groups. As discussed later, these functional groups can be easily modified to tune the solubility of the dendrimer. Functional groups on the dendrimer surface are also convenient handles for immobilizing DENs on solid supports, thereby enabling the use of DENs for applications in electrocatalysis and heterogeneous catalysis.

1.2 Nomenclature

Dendrimers are a class of regular, highly branched, and highly symmetrical polymers. For further details on the broad field of dendrimer chemistry the reader is referred to a recently published book.[25] Additional specialized reviews

are also available.[26-30] Here, some of the jargon that has evolved within the dendrimer community is summarized, and some background information that is essential for understanding DENs is also provided.

The generation of a dendrimer is the number of repeating branch points as traced from the dendrimer center to the periphery. PAMAM dendrimers range in generation from 0 to 10. The number of peripheral functional groups on the dendrimer increases exponentially with increasing generation whereas its diameter increases linearly. As a result, higher generation dendrimers exhibit structures with increasingly crowded peripheries and open cores containing voids.[31-34]

A dendrimer of generation *n* with terminal functional groups R is notated G*n*-R. Most studies of DENs have been carried out using G*n*-OH or G*n*-NH_2 (*n* = 4 or 6) PAMAM dendrimers, because these intermediate generation materials have a well-developed three-dimensional structure (which is essential for stabilizing the encapsulated nanoparticle) but are not so large as to have an overly crowded periphery. The metal-ion-dendrimer precursor complexes are denoted G*n*-R$(A^{m+})_x$, where *A* is the metal ion used, *m* is its oxidation state, and *x* represents the stoichiometric amount of *A* used in the synthesis. Monometallic and alloy bimetallic DENs are denoted as G*n*-R(A_x) and G*n*-R(A_xB_y), respectively, where *A* and *B* are the metals comprising the DENs, and *x* and *y*

represent the stoichiometry used in the synthesis. Core@shell bimetallic DENs are denoted as G*n*-R(A_x@B_y), where *A* and *B* are the metals comprising the core and shell materials, respectively. Typically, "magic number" values of *x* and *y* are chosen to yield nanoparticles having stable, closed shell structures. For instance, fcc cuboctahedral particles with one, two, and three complete shells contain 13, 55, and 147 atoms, respectively.

As mentioned previously, the PAMAM family of dendrimers is most frequently used for synthesizing DENs, and, unless otherwise indicated, the studies discussed in this dissertation refer to them. Note, however, that other types of dendrimers, such as the poly(propylene imine) (PPI),[35,36] phenylazomethine (DPA),[37,38] and triazole[39-41] families have also been used for this purpose. An important distinction can be made between dendrimer-stabilized nanoparticles (DSNs) and DENs. DSNs differ from DENs in that DSNs are not located within the voids of a single dendrimer, but rather are stabilized by the peripheral groups of the dendrimer. Therefore, DSNs are stabilized by multiple dendrimers and are usually quite a bit larger than DENs.

1.3 Synthetic Methods

As described previously, the basic synthesis of DENs is a two-step process where metal ions are first complexed to a dendrimer template and then reduced to form zerovalent particles contained within the dendrimer architecture.

However, there are several variations of this procedure that can be used to produce specialized DEN structures. Furthermore, details of the synthesis will vary depending on the specific metal system used. For instance, reactive metals, such as Ni,[42,43] Fe,[44] and Sn,[43] require synthesis in O_2-free organic solvents, and Pt DEN synthesis requires 2-3 days for the first complexation step and ~1 day for the subsequent reduction.[45] Details relevant to the DEN systems described in this dissertation are given in the relevant chapters.

Galvanic exchange. Galvanic exchange refers to an electrochemical process in which electrons transfer between two metals in different oxidation states and having different redox potentials (eq 1.1).

$$A(0) + B^{m+} \rightarrow A^{m+} + B(0) \qquad (1.1)$$

Here, metal *A* has a more negative standard potential than metal *B*. Galvanic exchange has previously been used for nanoparticle synthesis.[46,47] One example where this approach was used in the synthesis of DENs is a recent study where G6-OH(Cu_{55}) precursor nanoparticles were used to synthesize G6-OH(Pt_{55}) and G6-OH(Pd_{55}) DENs.[48] The details of this experiment are given here in order to illustrate the technique of galvanic exchange. The standard potentials for the relevant half reactions are given in eqs 1.2-1.4.[49]

$$Cu^{2+} + 2e^- = Cu(s) \qquad E^0 = 0.340\ V \qquad (1.2)$$

$$PtCl_4^{2-} + 2e^- = Pt(s) + 4Cl^- \qquad E^0 = 0.579\ V \qquad (1.3)$$

$$PdCl_4^{2-} + 2e^- = Pd(s) + 4Cl^- \qquad E^0 = 0.620\ V \qquad (1.4)$$

Note, however, that these potentials refer to the bulk metals, and the corresponding values for nanoscale particles are likely to be different.[19] Because the E^0 values of the Pt and Pd half reactions are more positive than Cu, electrons will spontaneously transfer from zerovalent Cu DENs to $PtCl_4^{2-}$ and $PdCl_4^{2-}$ (eqs 1.5 and 1.6, respectively).

$$G6\text{-}OH(Cu_{55}) + 55PtCl_4^{2-} \rightarrow 55Cu^{2+} + G6\text{-}OH(Pt_{55}) + 220Cl^- \qquad (1.5)$$

$$G6\text{-}OH(Cu_{55}) + 55PdCl_4^{2-} \rightarrow 55Cu^{2+} + G6\text{-}OH(Pd_{55}) + 220Cl^- \qquad (1.6)$$

Dialysis into an acidic solution after the galvanic exchange is completed allows for the removal of excess Cu^{2+} from the DEN solution. Characterization by transmission electron microscopy (TEM), extended X-ray absorption fine structure (EXAFS), UV-vis, and X-ray photoelectron spectroscopy (XPS) of the Pt and Pd DENs produced by this method indicate that a one-to-one exchange occurs between the reduced metal and the oxidized Cu during intradendrimer galvanic exchange.

The galvanic exchange method allows Pt DENs to be prepared in ~3 h, as compared to 96 h for the usual BH_4^--based Pt DENs synthesis (Scheme 1.1). Moreover, Pt DENs prepared by galvanic exchange are fully reduced, unlike

those prepared by the conventional chemical reduction method (vide infra).[45]

Bimetallic DEN Synthesis. There are a variety of methods that have been used to synthesize bimetallic DENs in both alloyed[10,11,43,50,51] and core@shell[12,52,53] configurations, including sequential reduction,[12] co-complexation,[10,11,43,50,51] and underpotential deposition (UPD).[52,53] The sequential reduction method involves synthesis of a monometallic DEN core followed by complexation and reduction of a second shell metal. In the co-complexation method, two or more metal salts are added to the dendrimer solution prior to reduction of the metal, typically resulting in an alloyed type structure. Details of the UPD method are given in Section 1.6.

Partial galvanic exchange of a metal nanoparticle has been proposed as a method to produce bimetallic DENs.[46] Specifically, addition of a substoichiometric amount of the more noble metal ions would result in exchange of just a fraction of the original DEN. This approach has been reported to yield bimetallic Pt@Au particles from Cu DEN precursors.[54] However, the resulting nanoparticles were larger than expected for DENs, and it seems likely they were actually DSNs.

1.4 Characterization of DENs

Accurate characterization of DENs is critical for correlating their structure and function. However, two of

the principal attributes of DENs, their small size and their location within the interior of a bulky hydrocarbon framework, make this task difficult. Accordingly, substantial effort has been focused on improving and expanding the methods available for characterizing DENs.

Structural Characterization of DENs. The structural characteristics of DENs include their crystallinity, degree of disorder, and, for bimetallics, degree of spatial segregation of the two metals. An understanding of surface structure is particularly important, because it can directly influence catalytic reactions.

The small size of DENs precludes structural characterization techniques that require long-range order, such as typical X-ray diffraction (XRD). However, EXAFS and X-ray diffraction-pair distribution function (XRD-PDF) are useful for analyzing even the smallest DENs. EXAFS provides information about the coordination environment of an absorbing atom, including the number, type, and bond distances of neighboring atoms. Further details about the technique are given in Section 2.3. EXAFS is particularly powerful for analyzing DENs, because the average coordination number (CN) drops precipitously as particle size decreases and a higher fraction of atoms reside on the particle surface. For example, surface-to-interior atom ratios for 147- and 55-atom cuboctahedra are 1.7 and 4.2, respectively, and therefore EXAFS is quite sensitive to

small changes in the size (and shape) of DENs.[55] XRD-PDF measures the distribution of mass in a sample and can be used to determine atomic structure in amorphous materials. The experimental PDF, G(r), is given by eq 1.7, where $\rho(r)$ and ρ_0 are the local and atomic number densities, respectively.

$$G(r) = 4\pi r(\rho(r)-\rho_0) \quad (1.7)$$

A recent study demonstrates the power of combining EXAFS with XRD-PDF and other analytical methods to solve complicated structural problems. In one particular case, the problem was that several studies suggested that the structure of Pt DENs was highly sensitive to the method used to prepare them.[8,45,56-59] This situation is in contrast to DENs synthesized from most other metals, which is quite straightforward. To better understand the products of the homogeneous-reduction method for preparing Pt DENs, a combination of EXAFS and XRD-PDF, as well as UV-vis spectroscopy, TEM, and XPS were used to characterize both dry and wet (solution-phase) G6-OH(Pt_x) (x = 55, 147, 240) DENs.[45] The XPS, UV-vis spectroscopy, and EXAFS data indicated incomplete reduction of the G6-OH(Pt^{2+})$_x$ precursor. For example, Figures 1.1a and 1.1b show the Pt-Pt CNs for dry and wet Pt DENs determined using EXAFS.

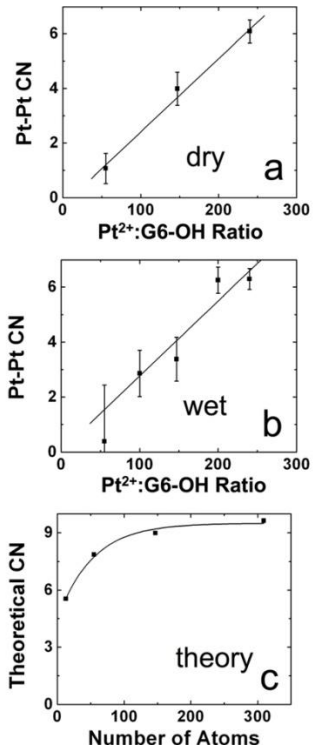

Figure 1.1.

Comparison of the Pt—Pt CNs for (a) dry and (b) wet Pt DENs at the indicated Pt^{2+}:G6—OH ratios. (c) Calculated M—M CNs for cuboctahedral particles in this size range. *Chem. Mater.* 2008, *20*, 5218-5228.

In both cases, the experimentally determined CNs are much lower than those expected on the basis of the precursor stoichiometry (Figure 1.1c). However, because EXAFS measures the average coordination environment of an element, it cannot distinguish between a mixture of configurations having high and low CNs and a single configuration having an intermediate CN. Taken together with the XPS and UV-vis spectroscopy results, one possible conclusion is that each

dendrimer contains some reduced Pt (in the form of a smaller-than-expected nanoparticle) and some unreduced Pt (in the form of the precursor complex in which the Pt-Pt CN=0). Interestingly, however, TEM micrographs indicated particle sizes close to those expected for fully reduced DENs.

To resolve this apparent inconsistency, XRD-PDF analysis was used, which confirmed the TEM results. Both XRD-PDF and TEM are insensitive to the presence of unreduced complex: only nanoparticles will be detected using these techniques. The only model that fit the results from all of these analytical methods is one in which some dendrimers contained fully reduced Pt DENs and others contained only the original precursor ions. This bimodal distribution model was rationalized by invoking a mechanism involving autocatalytic growth of the DENs. That is, zerovalent Pt seeds are formed by chemical reduction in some dendrimers, and these seeds catalyze complete reduction of all Pt^{2+} present in those dendrimers. However, in other dendrimers these seeds do not form, and hence no subsequent particle growth is observed.

Probes of DEN size. TEM is the most common method for measuring the size of DENs. Other standard characterization techniques for this size regime, for example atomic force microscopy (AFM), are hindered by the presence of the dendrimer shell.[60] Although TEM can be an effective means

for size determination, it suffers from three drawbacks. First, routine electron microscopy does not provide sufficient resolution to distinguish between particles having sizes that vary by just a few tens of atoms. Aberration-corrected microscopes should provide this level of resolution, but they have only recently become available and are still relatively inaccessible. Second, TEM samples are typically imaged in vacuum or a low-pressure gas, and this excludes (for now) liquid-phase, in-situ studies. Third, the sample configuration (for example, apparent agglomeration) can change during TEM sample preparation.

There are several indirect measures of particle size that corroborate the TEM findings. For example, the optical plasmon band of solution-phase DENs can be used to estimate, or least set an upper bound, on their size if they are comprised of appropriate metals, such as Ag, Au, or Cu.[61] For instance, Cu nanoparticles <3 nm in diameter do not exhibit a plasmon band in the UV-vis.[1] As mentioned earlier, size information may also be obtained from EXAFS data. This is because the ratio of surface to interior atoms increases significantly with decreasing size for particles <2 nm in diameter. Accordingly, the predicted CNs for cuboctahedral particles containing 55 and 147 atoms are 7.86 and 8.98, respectively, and such values can usually be distinguished.

The relative 1D ^{1}H-NMR peak intensities of the internal dendrimer functional groups are reduced by the presence of DENs. Figure 1.2 shows the methylene region of ^{1}H-NMR spectra for G4-OH, G4-OH$(Pd^{2+})_{55}$, and G4-OH(Pd_{55}), as well as peak assignments for the PAMAM dendrimer structure.

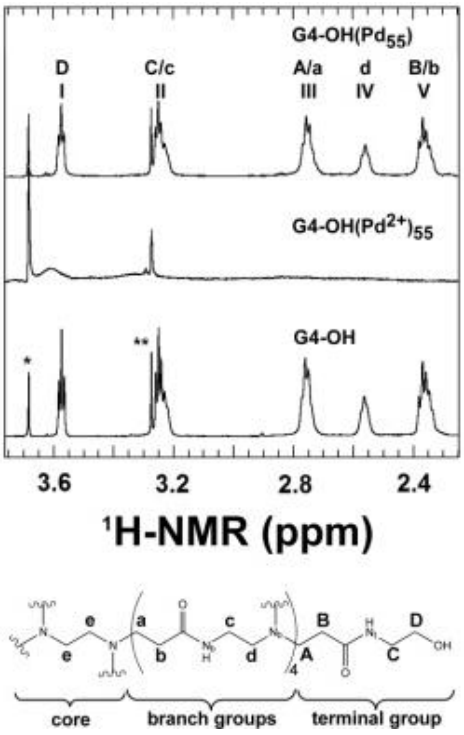

Figure 1.2.

(Top) ^{1}H NMR spectra of G4-OH, G4-OH$(Pd^{2+})_{55}$, and G4-OH(Pd_{55}). The peak marked with a single asterisk arises from the dioxane internal standard, and the peak marked with a double asterisk arises from residual methanol. (Bottom) Schematic representation of G4-OH indicating the lettering scheme used to identify the methylene and nitrogen groups.
J. Am. Chem. Soc. 2009, *131*, 341-350.

The peak assignments for G4-OH were made using a combination of ^{1}H, ^{1}H-^{1}H correlation spectroscopy (COSY) NMR, ^{1}H-^{15}N

heteronuclear multiple bond correlation (HMBC) NMR, ^{1}H-^{13}C heteronuclear single quantum coherence (HSQC) NMR, and ^{1}H-^{13}C HMBC NMR.[20]

Interestingly, a correlation exists between the size of DENs and the dampening of the NMR signal.[62] To demonstrate this principle, the D/d ratio (Figure 1.2) for G6-OH(Pd_x) (x = 55, 147, 200, 250) DENs were compared and found to scale linearly with particle size (Figure 1.3).

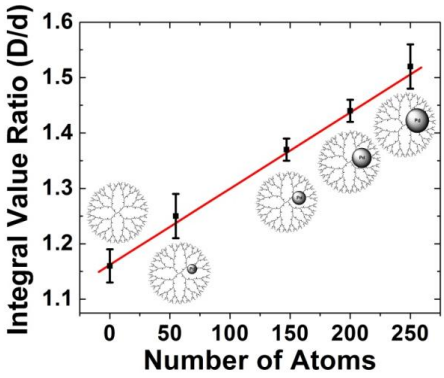

Figure 1.3.

Ratio of the integrated D/d peak intensities of ^{1}H NMR spectra for G6-OH(Pd_x) (x = 55, 147, 200, 250) as a function of the average number of atoms in the DENs. *J. Am. Chem. Soc.* 2009, *131*, 14634-14635.

This method of characterization may be useful for research groups without access to high-resolution TEM. Furthermore, this experimental method provides a means for in-situ analysis of DENs.

Mass spectrometry (MS) is a powerful method for determining the composition of small nanoparticles.[63] The ability of MS for measuring the size of DENs depends upon

the nature of the dendrimer encapsulating the particle. For example, Yamamoto and coworkers used matrix-assisted laser desorption/ionization-time of flight (MALDI-TOF) MS to measure the size of Rh DENs synthesized in G4 DPA dendrimers.[38] However, obtaining reliable MS spectra for high-generation PAMAM dendrimers, even in the absence of an encapsulated nanoparticle, is challenging.[64]

1.5 Evidence of Encapsulation

When DENs were first reported, evidence for encapsulation was circumstantial. However, support for this architecture was provided by an early TEM study of Au DENs.[13] In this study, the dendrimers were stained with a dye that provided electron contrast, so that colocalization of the nanoparticles and dendrimers could be confirmed. More recent studies of the spatial relationship between the DEN and the surrounding dendrimer have also appeared, and these are discussed next.

One of these studies monitored CO adsorption onto the surface of both dried and solution-phase Pt DENs in a variety of solvents.[65] It was found that in polar solvents CO adsorbed strongly and extensively to the DEN surface. However, dry DENs exhibited weaker adsorption and lower coverages of CO. This study concluded that in poor solvents (air and low dielectric liquids) the dendrimer collapses onto the surface of the encapsulated DEN and thereby shields it from interactions with adsorbates like CO. In contrast,

good solvents for the dendrimer expand its structure and permit interactions between small molecules and the encapsulated nanoparticle. These observations are only consistent with the nanoparticles being fully encapsulated within the dendrimer host.

A similar study used alkanethiols to carry out solvent-selective poisoning of the surface of Pt DEN catalysts.[57] In this case, hydroxyl-terminated DENs were immobilized onto an electrode surface and then exposed to alkanethiols in either polar or nonpolar solvents. In polar solvents, the alkanethiols strongly bound to the Pt DENs and inhibited electrocatalytic reactions. However, in nonpolar solvents, no poisoning was observed. The results were interpreted exactly as described in the previous paragraph, thereby providing additional evidence for nanoparticle encapsulation.

High-resolution NMR studies of Pd DENs also provide evidence for nanoparticle encapsulation.[20,62] As indicated in Figure 1.2, the peak positions of the peripheral methylene groups (those located closest to the terminal functional groups) are shifted relative to the peaks of the interior methylene groups. Interestingly, all of the ^{1}H peaks originating from the dendrimer disappear upon complexation of Pd^{2+}. This is likely a consequence of Pd^{2+} breaking the symmetry of the dendrimer. However, after reduction with BH_4^-, the dendrimer peaks return (with slightly decreased

intensity), but the relative intensity of the internal methylene peaks to those of the peripheral methylene peaks decreases. This suggests a partial breaking of the interior symmetry of the dendrimer. However, when the Pd DEN is extracted from the dendrimer using short-chain thiols, the peak intensities of the functional groups return to the initial free dendrimer values. This is strong evidence that the Pd particle is encapsulated by the dendrimer.

The final evidence for encapsulation was demonstrated using two techniques that measure changes to the hydrodynamic radius of the dendrimer after nanoparticle formation: pulsed-field gradient spin-echo (PFGSE) NMR[20,62] and quasi-elastic light scattering (QLS).[66] The PFGSE NMR results indicated a radius 2.0 ± 0.2 nm for both G4-OH and G4-OH(Pd_{55}),[20] and a radius 3.3 ± 0.3 nm for G6-OH and G6-OH(Pd_x) (x = 55, 147, 200, 250).[62] If the nanoparticle is truly encapsulated within the dendrimer, then the hydrodynamic radius of the dendrimer should not be affected by its presence. Clearly, that is the case here.

QLS was also used to determine the hydrodynamic radius of G6-OH(Pd_{147}), and under similar solution conditions the result (3.3 ± 0.3 nm) was the same as determined by PFGSE NMR.[66] Similar results were obtained for G6-OH(Au_{147}) (3.2 ± 0.2) and G6-OH(Pt_{147}) (4.0 ± 0.2 nm).[66] However, under certain solution conditions, primarily around neutral pH, the hydrodynamic radius of G6-OH(A_{147}) (A = Pd, Au, and Pt)

was found to nearly double, even though the size of the empty dendrimer (G6-OH) and the precursors examined (for example, G6-OH$(Pt^{2+})_{147}$) maintained a normal radius of around 3.5 nm. Importantly, there was no indication of aggregation in the TEM analysis of G6-OH(A_{147}) (*A* = Pd, Au, and Pt). Thus, the physical phenomenon responsible for the anomalous size increase, measured by QLS, of these DENs at neutral pH remains something of a mystery.

The surface metal atoms of DENs do not seem to be significantly passivated by the interior functional groups of the PAMAM dendrimer. Indirect evidence for this is given by the high catalytic rates exhibited by DENs.[14,57] Additionally, a recent EXAFS study of G6-OH(Au_{147}) DENs indicated an upper limit of 15 nitrogen or oxygen interactions with the metal surface.[21] This indicates at least 84% of the surface remains accessible for catalytic reactions.

1.6 Electrochemical Studies Utilizing DENs

As mentioned previously, the dendrimer can act as a convenient handle for attaching the DEN to surfaces. One of the earliest electrochemical studies utilizing DENs established a method for electrochemical attachment of hydroxyl-terminated DENs to a glassy carbon electrode (GCE).[57] Since this initial study, considerable effort has been focused on measuring size and composition dependent

electrocatalytic properties of DEN materials. UPD on DENs has also been used to produce novel DEN structures.

Electrocatalysis. In electrocatalysis, DENs are immobilized on an electrode surface, and the catalytic rate is measured as a function of the electrode potential. As for all forms of DEN-based catalysis, the reactants must permeate the dendrimer periphery and interact directly with the surfaces of the encapsulated DENs. However, in electrocatalysis, electrons from the electrode must also access the nanoparticles. How exactly this happens has not been explored, but the fact that it does happen is unambiguous.

One early study of DEN-based electrocatalysis examined the effect of nanoparticle size on the kinetics of the oxygen reduction reaction (ORR).[67] Specifically, G6-OH(Pt_x) (x = 55, 100, 147, 200, 240) DENs were immobilized on a glassy carbon rotating disk electrode (GC RDE), and the specific activity of each size DEN was determined using standard electrochemical methods.[57] The results indicated that the kinetics of the ORR decreased monotonically with decreasing particle size. It is a testament to the DENs synthetic method that significant and reproducible differences in ORR kinetics are observed when particle sizes are changed by just a few tens of atoms. Interestingly, the smallest two DENs exhibited decreased mass-transfer limited currents, which could represent a change in the product of

the ORR from water to peroxide. Note, however, that there are alternative explanations for this observation.

The ORR kinetics of bimetallic PtPd alloy DENs always containing ~180 atoms but at different ratios of the two metals was also examined.[11] The PtPd DENs were synthesized using the co-complexation technique and immobilized onto the surface of a GC RDE. The kinetic analysis revealed two important results. First, Tafel plots suggested that the ORR mechanism was the same for PtPd DENs having different elemental compositions. Second, when normalized to the mass of Pt present in each composition, DENs containing Pd:Pt atomic ratios of 30:150 and 60:120 exhibited superior activities compared to Pt-only DENs.

Some years ago it was shown that positively charged amine-terminated dendrimers immobilized onto an electrode surface can act as molecular gates, blocking access of positively charged species in solution while permitting negatively charged ions to access the substrate.[68] This effect was attributed to electrostatic interactions between the redox probes and the positive charges on the protonated dendrimer. Kim and coworkers used this effect to confirm immobilization of amine-terminated Au DENs onto a GCE.[69] Immobilized G6-NH_2(Au_{147}) DENs were also used in this study to catalyze hydrazine oxidation.

In addition to catalysis on planar electrodes, several groups have immobilized DENs on carbon nanotubes (CNTs),

which serve as conductive leads to an electrode surface. For example, Stevenson and co-workers outfitted nitrogen-doped CNTs with Pt DENs contained within amine-terminated dendrimers and used the supported nanoparticles to catalyze the ORR.[70] Centrifugal separation and UV-vis spectroscopy were used to monitor adsorption of the DENs onto the CNTs. Adsorption isotherms revealed that the affinity of the Pt DENs for the CNTs increased with increasing edge-plane character. In another study, G4-NH_2(Pd_{40}) DENs were anchored to chemically oxidized multi-walled nanotubes (MWNTs) through covalent attachment of the terminal amine groups to carboxyl groups on the nanotube.[71] These materials were found to be catalytically active for hydrazine oxidation.

Underpotential Deposition. UPD is normally thought of as the reductive electrodeposition of cations at potentials more positive than their standard potential.[72] This method provides high surface selectivity and can be used to synthesize core@shell nanoparticles having a single atomic layer shell or in some cases a submonolayer shell.[73-76] Furthermore, the UPD monolayer can subsequently be galvanically exchanged for a more noble metal, thereby expanding the scope of this method.[73-75,77] The use of UPD for synthesizing nanoparticles having core@shell structures was pioneered by Adzic and coworkers, particularly for synthesizing ORR electrocatalysts having low Pt

loadings,[73,74,77] and Carino et al. has adopted this same general approach for synthesizing core@shell DENs.[52,53]

The UPD method was used to deposit a single monolayer of Cu onto Pt DENs comprised of 55-225 atoms.[52] The synthesis is carried out by preparing the Pt DEN cores, immobilizing them onto a GCE,[57] and then depositing a monolayer of Cu onto their surface via UPD. As shown in Figure 1.4, a voltammetric wave having two distinct reduction peaks is observed for UPD onto the largest Pt core, but only a single broad peak is present for the two smaller cores.

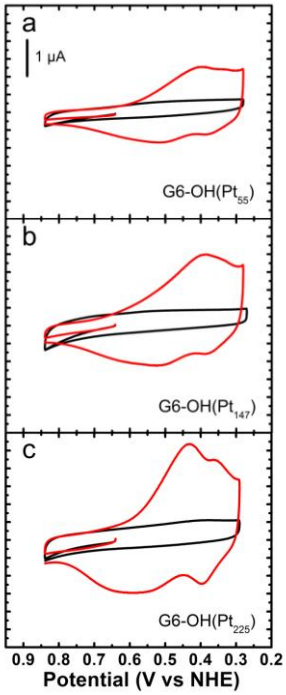

Figure 1.4.

Cyclic voltammograms obtained using GCEs modified with the indicated G6-OH(Pt_x) DENs in aqueous electrolyte solutions containing 0.10 M H_2SO_4 only (black) and 0.10 M H_2SO_4 + 0.010 M $CuSO_4$ (red). The Cu UPD potential region is shown. The solutions were deoxygenated with Ar. The scans started at 0.64 V and were initially swept in the positive direction at a rate of 10 mV/s. *Langmuir* **2011**, *27*, 4227-4235.

This suggests that the UPD process is better defined on the larger, more highly faceted core. That is, as the size of the facets increase, UPD occurs at distinct potentials on the 111 and 100 facets of the DENs.

The ratio of Cu shell atoms to Pt atoms on the surface of the core, which is denoted θ_{Cu}, was determined by comparing the Pt surface area, measured by H-atom

desorption,[78] to the amount of Cu deposited. The latter value was found by integrating the area under the Cu UPD peaks and converting this charge to total moles of Cu. The value of θ_{Cu} is 1.0 for 147- and 225-atom Pt DEN cores, but θ_{Cu} = 1.5 for the 55-atom cores. Note that complete Cu shells for cores containing 55, 147, and 225 Pt atoms have θ_{Cu} values of 2.2, 1.8, and 1.7, respectively. This suggests that only the facets of the two larger DENs are decorated with Cu, while the facets, edges, and corner sites are all covered on the 55-atom core. As discussed later, EXAFS was also used to confirm the core@shell structure of the DENs.

In a separate UPD study, G6-OH(Au_{147}) DENs were immobilized on a GCE followed by UPD of a Cu monolayer.[53] Galvanic exchange of the Cu monolayer for Pt resulted in Au@Pt DENs. The surface composition of these particles was determined by integrating the voltammetric peaks associated with reduction of surface Au oxide and Pt oxide. The Pt shell coverage, θ_{Pt}, was calculated as 0.85 by this method. The activity of these particles toward the ORR was very close to that of G6-OH(Pt_{147}) DENs synthesized by the usual BH_4^- reduction method.

Chapter 2: Experimental

2.1 Chemicals

Specific information about the chemicals used in the dissertation is given in the following chapters.

2.2 Methodology

The synthesis of Pd, Cu, and alloyed PdCu DENs is described in chapters 3 and 5. Chapter 4 details the synthesis of Pt DENs. Descriptions of the EXAFS fitting procedures used in these studies are described in chapters 3 and 4. A spectroelectrochemical cell was designed for in-situ X-ray absorption spectroscopy (XAS) characterization during electrochemical experiments. A detailed description of the cell is provided in chapter 4. The preparation of DEN-immobilized working electrodes are detailed in chapters 4 and 5. Experimental details for the techniques utilized in this dissertation are given in the following chapters.

2.3 Extended X-ray Absorption Fine Structure

In an EXAFS experiment, information about the coordination environment of an absorbing element is extracted from the oscillations present in an X-ray absorbance spectrum. Absorption of an X-ray photon by a material at sufficiently high energies results in the ejection of a core electron. Atoms surrounding the

absorbing material may cause backscatter of the ejected electron, leading to interference between the backscattered wave and the outgoing wave of the ejected electron, and resulting in a fine structure in the absorbance spectrum. The fine-structure function, $\chi(E)$, is defined in eq. 2.1.

$$\chi(E) = (\mu(E) - \mu_0(E)) / \Delta\mu_0(E) \quad (2.1)$$

Here, $\mu(E)$ is the absorption coefficient, $\mu_0(E)$ is an absorption background describing the absorption of a free atom in space, and $\Delta\mu_0(E)$ is the jump in absorption at the threshold energy of absorption. The finite lifetime of the ejected electron ensures that EXAFS is essentially a short-range order technique, making it a complementary method to other structural characterization methods, such as XRD.

Interpretation of an EXAFS spectrum is achieved through least square fitting of the data to appropriate theoretical models using the EXAFS equation, which describes the energy-dependent absorbance of a material as a sum of the individual contributions of j coordination shells (eqs. 2.2-2.3).

$$\chi(k) = \sum_j (N_j S_0^2 f_j(k) e^{-2k^2\sigma_j^2} (kR_j^2)^{-1} \sin(2kR_j + \delta_j(k))) \quad (2.2)$$

$$\text{Where } k^2 = 2m_e(E-E_0)\hbar^{-1} \quad (2.3)$$

Here, N_j is the number of atoms in each coordination shell, S_0^2 is the passive electron reduction factor, R_j is the bond

distance between the absorbing atom and the nuclei in the coordination shell, f_j is effective scattering amplitude, σ_j^2 is mean square displacement of the bond distances, $\delta_j(k)$ is the effective scattering phase shift, and E_0 is the absorption-edge energy.

One approximation made in the EXAFS equation is that any interactions between the ejected electron and the valence electrons of the absorbing atom are negligible. This assumption only holds true when the kinetic energy of the outgoing electron is sufficiently higher than the electronic energies of the valence electrons. Therefore, EXAFS describes the region of the absorbance spectrum greater than several tens of eV above the absorption edge.

Illustration 2.1 diagrams the basic components of the XAS beamline used for the studies detailed in this dissertation.

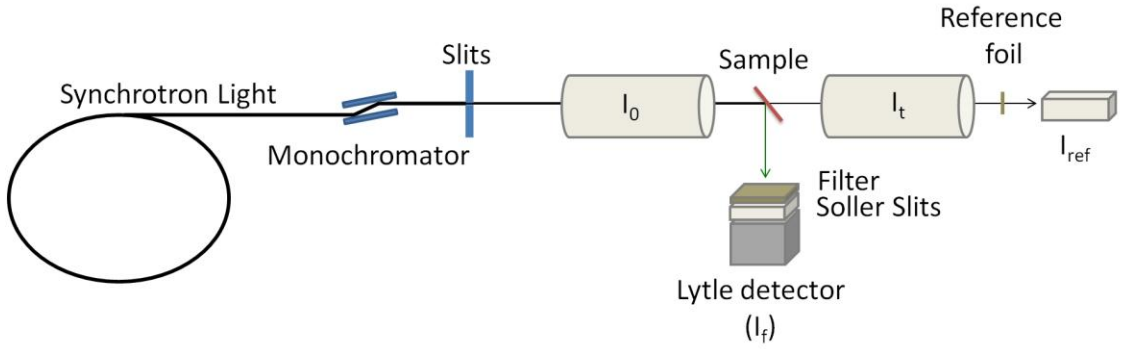

Illustration 2.1.

Broadband light is collected tangentially from a synchrotron ring. A double-crystal Si(111) channel-cut monochromator selects for a single wavelength of light. A series of slits are used to control the spot size of the beam on the sample and improve energy resolution of the light source. There are four gas-ionization detectors which are filled with a gas that becomes ionized when electromagnetic radiation passes through them. By measuring a current produced by the charged gas, it is possible to determine the intensity of the light passing through the chamber. I_0 and I_t measure the intensity of the beam before and after, respectively, passing through the sample. The absorbance by the sample is given in eq. 2.4, where *t* is the sample thickness.

$$\mu(E) = \ln(I_0/I_t)/t \tag{2.4}$$

A third detector, I_{ref}, is used to measure the absorbance by a reference sample, which is used to accurately calibrate the energy of the X-ray beam.

Fluorescence data may be collected when insufficient signal to noise is present in the transmission spectrum. Filling of the core-hole vacancy formed during the X-ray absorption event results in the emission of a lower-energy photon. This fluorescence of the sample is related to μ(E) by the following relationship (eq. 2.5).

$$\mu(E) \propto I_f/I_0 \tag{2.5}$$

The fluorescence detector is placed at a 90˚ angle to the X-ray beam. A set of Soller slits and an appropriate filter help to prevent inelastically scattered photons from hitting the detector.

Chapter 3: An X-ray Absorption Study of PdCu Bimetallic Alloy Nanoparticles Containing an Average of ~64 Atoms

3.1 Introduction and Background

In this chapter the synthesis and characterization of PdCu bimetallic alloy nanoparticles consisting of an average of ~64 atoms is presented. It has been shown that such materials, composed of electron donor and acceptor metals, can exhibit desirable catalytic properties for the ORR.[79-82] Specifically, when an electron donor atom, such as Cu, is present in the core, and an electron acceptor, such as Pd, is present in the shell, then the d-band of the shell is lowered and its local electronic properties are predicted to be more like Pt. However, first-principles calculations are only available for particles containing small numbers of atoms (typically <~150). Accordingly, there is an urgent need to prepare well-defined, bimetallic nanoparticles in this size range that consist of both donor and acceptor elements.

The nanoparticles discussed here were prepared by co-complexation of Pd^{2+} and Cu^{2+} salts to interior functional groups of a dendrimer template followed by chemical reduction to yield DENs. EXAFS spectroscopy indicates that the particles have the expected alloy structure. Thus, although these materials are alloys rather than core@shell nanoparticles, the findings presented here are an important

first step toward the eventual goal of synthesizing and characterizing very well-defined nanoparticles whose electrocatalytic properties can be directly compared to theory.

There has been one previous study of unsupported PdCu nanoparticles in the size range relevant to the present report. Specifically, Asakura and coworkers used EXAFS to characterize the structure of polymer-stabilized PdCu alloy nanoparticles dispersed in a glycol solution.[83] A preference for hetero-bond formation between the two metals was observed. There has also been one EXAFS study of supported PdCu bimetallic nanoparticles having diameters in the 2-6 nm range.[84] These materials were prepared by either an atomic layer epitaxy technique or by co-impregnation of the metals onto SiO_2 and γ–Al_2O_3 supports. The results indicated that the structure of the particles was dependent on the properties of the support: nanoparticles prepared on silica substrates had an alloyed structure whereas particles on alumina exhibited surface segregation of the Cu.

In this study, EXAFS was used a probe for distinguishing between certain bimetallic structures. Specifically, small core@shell, alloyed, and cluster-on-cluster nanoparticles have differentiable homo and hetero metal-metal CNs. This method has also been used to investigate the structures of PdAu[12,50] and PtCu[52] bimetallic DENs. For example, 147-atom PdAu DENs having different

Pd:Au ratios were synthesized using two different methods: co-complexation and sequential reduction.[12,50] EXAFS suggested that DENs synthesized using the co-complexation approach are quasi-random alloys (alloys with partial surface segregation of Pd), whereas DENs prepared by sequential reduction have a core@shell type structure. Further details of using EXAFS to distinguish bimetallic structures are given in the Results and Discussion section of this chapter.

In the present study, Pd^{2+} and Cu^{2+} salts were added to a dilute solution of G6-OH at five different ratios of Pd^{2+}:Cu^{2+}. The total metal-ion-to-dendrimer content was fixed at 64:1, because this ratio represents the maximum loading of Cu^{2+} ions into the interior of G6-OH PAMAM dendrimers.[1] UV-vis absorption spectra indicate complete complexation of the metal salts to the dendrimer. The metal-ion-dendrimer precursor complex was reduced with BH_4^-, which yielded DENs having diameters in the range of 1.2 - 1.3 nm as measured by TEM. The coordination environments of the two metals were measured by EXAFS and fit those of an alloy structure. The particle size was also estimated from the EXAFS data and was found to be in good agreement with the TEM results.

3.2 Experimental

Chemicals. G6-OH dendrimers in methanol were purchased from Dendritech, Inc (Midland, MI). The methanol

was removed by vacuum evaporation at 23±3 °C prior to use and either a 100.0 μM or a 500.0 μM aqueous stock solution was prepared. K_2PdCl_4 and $NaBH_4$ were purchased from Sigma-Aldrich. $CuSO_4$ was purchased from Fisher Scientific. All chemicals were used without further purification. 18 MΩ·cm Milli-Q deionized water was used to make all solutions.

Synthesis of alloy PdCu DENs. Bimetallic DENs having different ratios of Pd:Cu are denoted as G6-OH($Pd_xCu_{(64-x)}$) (*x* = 64, 48, 32, 16, 0). Note, however, that these nominal representations of DEN composition represent the average number of metal atoms in each DEN based upon the ratio of metal salts used to prepare the precursor complexes. Previous single-particle energy dispersive X-ray spectroscopy (EDS) studies of bimetallic DENs have demonstrated that the composition of individual particles is quite close to this ratio.[11] However, due to the difficulty of imaging PdCu DENs in the TEM used for EDS studies it was not possible to obtain reliable EDS data.

DENs were prepared by the following co-complexation method.[85] A sufficient aliquot of 10.0 mM K_2PdCl_4 was added to an aqueous G6-OH solution to yield the desired Pd^{2+}:G6-OH ratio. This mixture was stirred for 10 min to permit complexation of Pd^{2+} to the interior tertiary amines of the dendrimer.[86] Next, sufficient 10.0 mM $CuSO_4$ was added to this solution to give the desired Pd^{2+}:Cu^{2+} ratio. This solution was stirred for 5 min, and then the pH was adjusted

with NaOH to the optimal range for Pd^{2+} and Cu^{2+} complexation: between 7 and 8. The final dendrimer concentration was either 2.0 or 100.0 µM. The solution was bubbled with N_2 for a minimum of 10 min, and then 10 molar equivalents of $NaBH_4$ (relative to the total metal content) were added to the solution.

Characterization. UV-vis absorbance spectra were obtained using a Hewlett-Packard HP8453 spectrometer and a 1.00 cm pathlength quartz cuvette. A solution of G6-OH in water was used for background correction.

TEM images were collected using a JOEL-2010F TEM operating at 200 kV. Images were collected in transmission as well as high angle annular dark field scanning transmission electron microscopy (HAADF-STEM) mode. TEM grids were prepared by dropping several microliters of a 2.0 µM DEN solution onto a carbon-coated 400-mesh Cu grid (EM Sciences) and drying in air.

EXAFS data were collected on beamline X18b at the National Synchrotron Light Source (NSLS) at the Brookhaven National Laboratory (BNL) in New York. 100.0 µM solutions of freshly reduced DENs were placed in 1 cm thick solution cells having Kapton tape windows. The K absorption edges of Pd and Cu were measured simultaneously in transmission and fluorescence modes, by orienting the sample 45˚ relative to the beam. A five-grid Lytle detector filled with Ar gas was used for fluorescence detection, and, in the case of the Cu

K-edge, Soller slits and a Ni filter were used. At least two, and as many as eight, energy scans were averaged to improve the signal-to-noise ratio. Pd and Cu foil reference spectra were collected concurrently with the DENs spectra at the Pd and Cu K-edge, respectively, and used for energy calibration. The data were analyzed using the IFEFFIT software package and FEFF6 program.[87,88] The details of the data modeling procedure for monometallic and bimetallic systems are presented below.

3.3 Results and Discussion

UV-vis analysis of Cu, Pd, and PdCu DENs. Figure 3.1a contains UV- vis absorption spectra of 2.0 μM aqueous solutions of G6-OH$(Pd^{2+})_x(Cu^{2+})_{64-x}$ (x = 64, 48, 32, 16, 0) before reduction with BH_4^-.

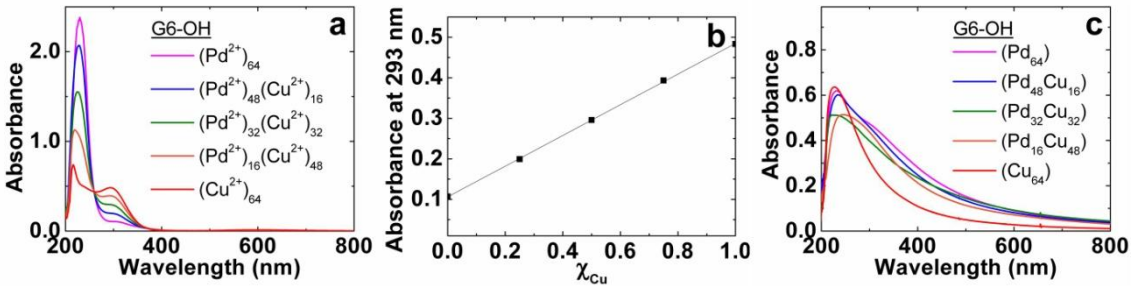

Figure 3.1.

(a) UV-vis absorption spectra for 2.0 μM G6-OH$(Pd^{2+})_x(Cu^{2+})_{(64-x)}$ (x = 64, 48, 32, 16, 0) complexes. (b) Absorbance of G6-OH$(Pd^{2+})_x(Cu^{2+})_{(64-x)}$ complexes at λ_{max} for the Cu^{2+} LMCT peak. (c) Spectra of the G6-OH$(Pd^{2+})_x(Cu^{2+})_{(64-x)}$ complexes after reduction with BH_4^-. The optical pathlength of the cuvette was 1.00 cm. 2.0 μM G6-OH was used as the background.

The DEN precursor solutions exhibit strong absorption bands at ~230 and 290 nm and an isosbestic point at 261 nm. These peaks arise from ligand-to-metal charge-transfer (LMCT) bands associated with the dendrimer/metal-ion complexes.[1,86] Pd^{2+} salts not associated with the dendrimer absorb in this region, and therefore the presence of an isosbestic point implies that all of the Pd^{2+} salts have complexed to the dendrimer interior. The absorbance data for G6-OH$(Cu^{2+})_{64}$ and G6-OH$(Pd^{2+})_{64}$ are comparable to previously published results.[1,86]

The optimal pH range for complexation of the metal salts to the dendrimer was found to be between 7 and 8. Complexation of Cu^{2+} is pH dependent due to competition of H^{+} for binding sites at low pH.[9,89] At high pH values, loss of Pd from the complex is observed. In the pH range used for this study, the absorbences of the LMCT bands of the bimetallic precursors are proportional to the mole ratios of Pd^{2+} and Cu^{2+} present in the dendrimers (Figure 3.1b). This finding provides additional evidence that the metal salts completely bind to the dendrimer.

Following chemical reduction of the G6-OH$(Pd^{2+})_{x}(Cu^{2+})_{64-x}$ complexes, the LMCT bands are replaced by broad, monotonically decreasing bands (Figure 3.1c) characteristic of interband transitions of spherical metal nanoparticles.[90] The irregular behavior below 230 nm is caused by the high absorbance of the dendrimer in this region. The absence of

a plasmon at 570 nm in the monometallic copper sample indicates a particle diameter below 3 nm,[91] because damping of plasmon absorption bands is observed when particle sizes are smaller than the mean free path of conduction electrons in the absorbing metal.[90] It is not clear why the spectra do not exhibit a consistent trend as a function of particle composition, but this observation may reflect the fact that these alloys have unique optical properties that are not a simple sum of the properties of the component metals.

If the DENs are stored in a reducing atmosphere, such as a H_2-saturated aqueous solution, they are stable and their absorbance spectra do not change as a function of time. However, non-reducing environments, like air-saturated water, result in partial DEN oxidation and gradual regrowth of the LMCT bands. This observation is consistent with other studies,[92] although the exact mechanism of oxidation is not fully understood. Dry Pd DENs are stable in the presence of air, but Cu DENs oxidize in air even when dry.

TEM analysis of Pd and PdCu DENs. The small size of these ~64-atom PdCu DENS, in conjunction with the low mass of Cu, make it difficult to obtain high-quality, bright-field TEM images. Therefore, particle diameters were estimated from HAADF-STEM micrographs. Due to their instability in air, it was not possible to obtain TEM images

of Cu monometallic DENs. Figures 3.2a and 3.2b show representative TEM images of the G6-OH($Pd_{32}Cu_{32}$) particles.

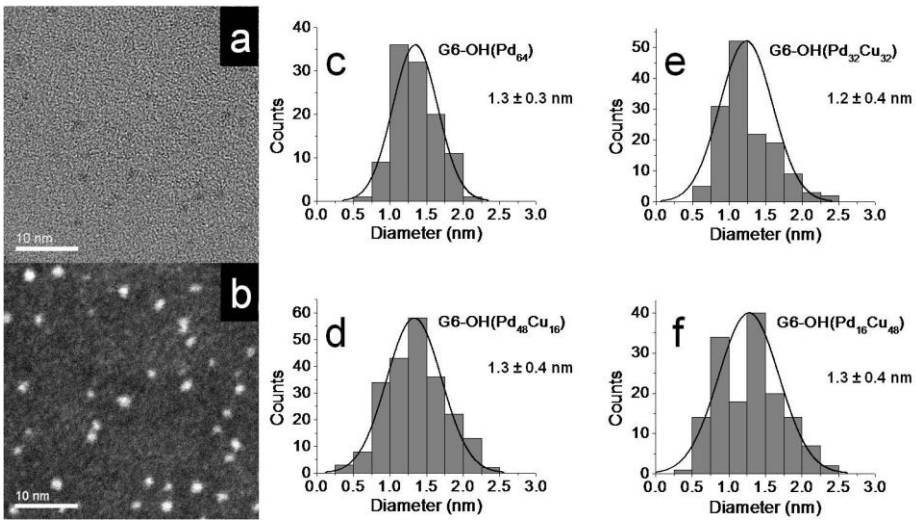

Figure 3.2.

(a) Bright-field TEM micrograph and (b) HAADF STEM micrograph for G6-OH($Pd_{32}Cu_{32}$). Particle size distribution for (c) Pd monometallic and (d-f) PdCu bimetallic DENs.

Theoretical particle sizes are estimated to be 1.4 and 1.3 nm for monometallic Pd and Cu particles, respectively, assuming a spherical geometry. Histograms of the measured particle diameters are provided in Figures 3.2c-f, and they indicate that the measured particle diameters are just slightly smaller (1.2 – 1.3 nm).

EXAFS fitting procedure. The fits were constrained to include only the first coordination shells. This eliminates all multiple-scattering effects and significantly reduces the number of independent variables. S_0^2 values were taken from fits to Pd and Cu reference foil data collected under

similar conditions on beamline X18b. A k-weight of 2 was used for all fits.

Metal-metal (M-M) and metal-low Z (M-E, *E* = C, O, N) interactions were included in the preliminary simulations. Cu-E interactions were found to be well below the uncertainty of the fit, and therefore they were not included in the final models for the Cu edge of the monometallic and bimetallic DENs. The CNs for Pd-E (n_{PdE}) are close to the uncertainty level of the fits for all DENs studied, but better fit values consistently resulted when Pd-E interactions were included. Further studies would be required to meaningfully quantify low-Z coordination to Pd.

The data from both metal edges of the bimetallic materials were fit simultaneously. The Pd-Cu (n_{PdCu}) and the Cu-Pd CNs (n_{CuPd}) were fixed according to eq 3.1.[93]

$$n_{PdCu} = \chi_{Cu} \chi_{Pd}^{-1} n_{CuPd} \qquad (3.1)$$

The heterometallic bond lengths and the σ^2 factors were also constrained to be the same as measured from each edge (Pd or Cu).

EXAFS analysis of monometallic Pd and Cu DENs. As discussed earlier, G6-OH($Pd_xCu_{(64-x)}$) DENs are only stable in reducing environments. Therefore, to prevent oxidation of the DENs during EXAFS experiments, the precursor complexes were reduced with BH_4^- immediately prior to data collection. In addition to reducing the precursor ions to DENs, BH_4^-

also slowly reduces water to H_2. The presence of H_2 in the DEN solutions throughout the period required to obtain EXAFS spectra, as evidenced by continuous bubble formation, ensured the integrity of the DENs. Indeed, UV-vis spectroscopy experiments carried out under nearly identical conditions to those used at the beamline confirmed that no regrowth of the LMCT bands occurred. More significantly, the EXAFS analysis, discussed later, indicates minimal oxide formation under these conditions.

Figure 3.3 shows the measured EXAFS data for the monometallic Pd and Cu DENs and theoretical fits of the first nearest neighbor contributions.

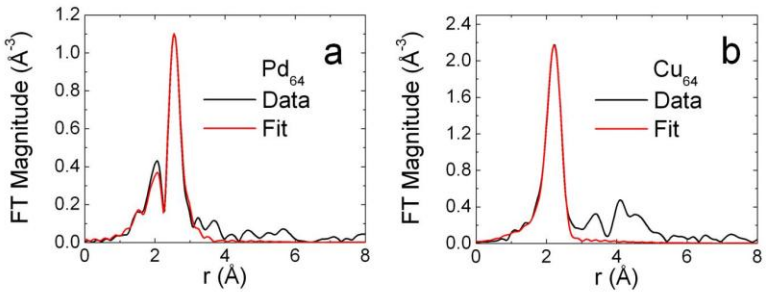

Figure 3.3.

EXAFS data (black) and simulated fits (red) for (a) G6-OH(Pd_{64}) and (b) G6-OH(Cu_{64}).

The selected *k*-ranges and *R*-ranges for each edge as well as the number of variables from each fit are given in Table 3.1.

Fitting parameters for PdCu DENs.

G6-OH	n_{ind}*	n_{var}+	k-range (Å^{-1})		R-range	
			Pd	Cu	Pd	Cu
Cu_{64}	14	4	-	2-14	-	1-2.8
$Pd_{16}Cu_{48}$	20	14	2-11	2-13	1.2-2.9	1.5-3
$Pd_{32}Cu_{32}$	21	14	2-12	3-12	1.2-2.9	1.1-3
$Pd_{48}Cu_{16}$	20	14	2-12	2-10	1.3-2.9	1-3
Pd_{64}	13	7	2-14	-	1.3-3	-

* number of independent data points
\+ number of fit variables

Table 3.1.

The CNs obtained from the fits, together with their 95% confidence limits (error bars) are presented in Table 3.2.

First-shell coordination numbers for PdCu DENs.

G6-OH	n_{CuCu}	n_{CuPd}	n_{PdPd}	n_{PdE}
Cu_{64}	7.1(4)	-	-	-
$Pd_{16}Cu_{48}$	4.2(8)	1.3(4)	3.5(2.0)	1.9(9)
$Pd_{32}Cu_{32}$	3.0(1.1)	3.1(5)	4.1(1.3)	0.8(4)
$Pd_{48}Cu_{16}$	0.9(7)	4.8(1.9)	4.0(1.4)	1.4(5)
Pd_{64}	-	-	6.5(4)	0.2(2)

Table 3.2.

A discussion of these results is given below. The full set of fitting results is provided in Table 3.3.

EXAFS Fitting Parameters

G6-OH	Cu_{64}	$Pd_{16}Cu_{48}$	$Pd_{32}Cu_{32}$	$Pd_{48}Cu_{16}$	Pd_{64}
ΔE_{0Pd} (eV)	-	-2.8(3.1)	-7.3(1.2)	-4.9(2.6)	-1.2(0.4)
ΔE_{0Cu} (eV)	2.3(0.5)	0.0(1.2)	-2.9(1.1)	1.0(1.8)	-
R_{Cucu} (Å)	2.527(3)	2.49(1)	2.47(1)	2.45(3)	-
R_{PdCu} (Å)	-	2.58(2)	2.57(1)	2.59(3)	-
R_{PdPd} (Å)	-	2.70(3)	2.68(2)	2.68(3)	2.779(3)
R_{PdE} (Å)	-	1.91(3)	1.93(2)	1.97(2)	1.96(3)
σ^2_{CuCu} ($Å^2$)	0.0093(5)	0.012(2)	0.012(4)	0.004(7)	-
σ^2_{CuPd} ($Å^2$)	-	0.011(3)	0.011(2)	0.017(8)	-
σ^2_{PdPd} ($Å^2$)	-	0.014(7)	0.015(4)	0.014(3)	0.0098(5)
σ^2_{PdE} ($Å^2$)	-	0.050(6)	0.000(4)	0.001(3)	0.001(6)
χ^2_{red}	2.4	4.6	2.7	10.5	3.2
R factor	0.001	0.008	0.011	0.022	0.006

Table 3.3.

As discussed previously, the total metal-metal CN (n_{MM}) can be used to estimate the size of DENs, because as particle size decreases the ratio of low-coordination surface atoms to interior atoms increases and therefore the total metal-metal coordination decreases. Such method can be used only if independent information about the particle

shape is available, as in this case, where it is known that the particles are quasi-spherical. The cuboctahedron cluster family was chosen to model CNs, because the values can be easily calculated for different cluster orders.[55,94-96]

The Pd and Cu monometallic DENs have n_{MM} values of 6.5 ± 0.4 and 7.1 ± 0.4, respectively (Table 3.2). The theoretical fcc cuboctahedron first shell n_{MM} values for 13-, 55-, and 147-atom particles are 5.54, 7.86, and 8.98, respectively. Larger particles will have a CN approaching the bulk value of 12. Predicting a theoretical CN for a 64-atom particle is more difficult, because it does not have a complete outer shell. It is reasonable for a particle of this size to have a lower coordination number that a 55-atom structure because the extra 9 atoms (of the 64-atom particle) will be low-coordinated surface atoms. Therefore, the sizes of the monometallic DENs, as judged from the CNs, are fully consistent with the TEM data and calculated values.

Because the samples are maintained in a reducing environment, Pd hydride formation is possible. The Pd-Pd bond lengths were measured at 2.78 Å, a 1.1% expansion over the bulk value for metallic Pd. This is consistent with the formation of the hydride in particles of this size.[97] However, the bimetallic nanoparticles did not exhibit this behavior (Table 3.3).

EXAFS analysis of bimetallic G6-OH($Pd_xCu_{(64-x)}$) DENs. As discussed in the introduction of this chapter, the CNs for each metal in small, bimetallic particles can yield information about the structure of the material.[55] For example, if metal atoms of type A segregate to the interior of a particle containing atom types A and B, the CN n_{AM} of neighboring atoms to A will be larger than n_{BM} since the majority of atoms on or near the particle surface are of the type B, which see fewer neighbors, on the average, than A. The distribution of CNs obtained for all types (A-M and B-M) of interactions between the two metals can reveal core@shell structure (when the n_{AM} and n_{BM} are different) or the homogeneous alloy structure (when they are similar, within the uncertainties). Finally, for a bimetallic material, the CN n_{AB} that quantifies the coordination of atoms A by atoms B will increase with increased alloying of the two metals.

The EXAFS data and simulated results for the bimetallic DENs are shown in Figure 3.4.

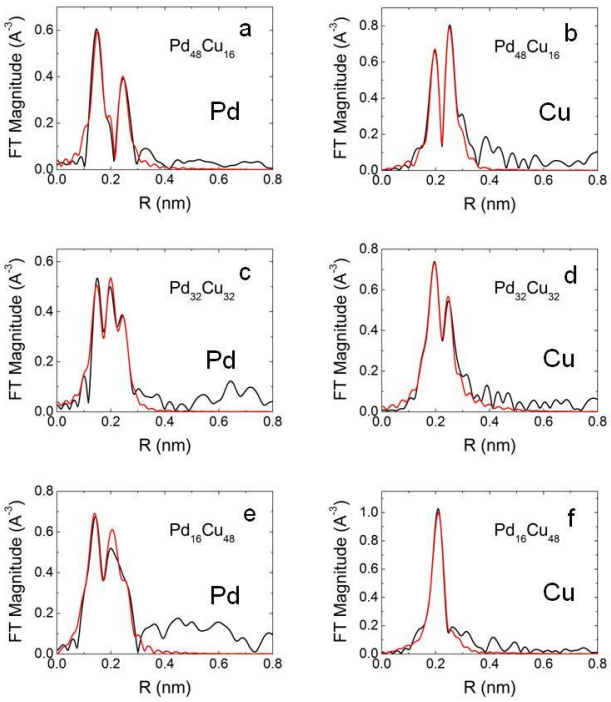

Figure 3.4.

EXAFS data and fit results for the (a) Pd K edge and (b) Cu K edge of G6-OH($Pd_{48}Cu_{16}$), (c) Pd K edge and (d) Cu K edge of G6-OH($Pd_{32}Cu_{32}$), and (e) Pd K edge and (f) Cu K edge for G6-OH($Pd_{16}Cu_{48}$). The data are plotted in black and the simulated fits are in red.

The CNs obtained from the fits are given in Table 3.2. The data indicate that the two metals in the bimetallic DENs are mostly alloyed. As shown in Figure 3.5a, the Pd-M CN (n_{PdM}) is the same or slightly higher than that of the Cu-M CN (n_{CuM}) for all three DEN compositions.

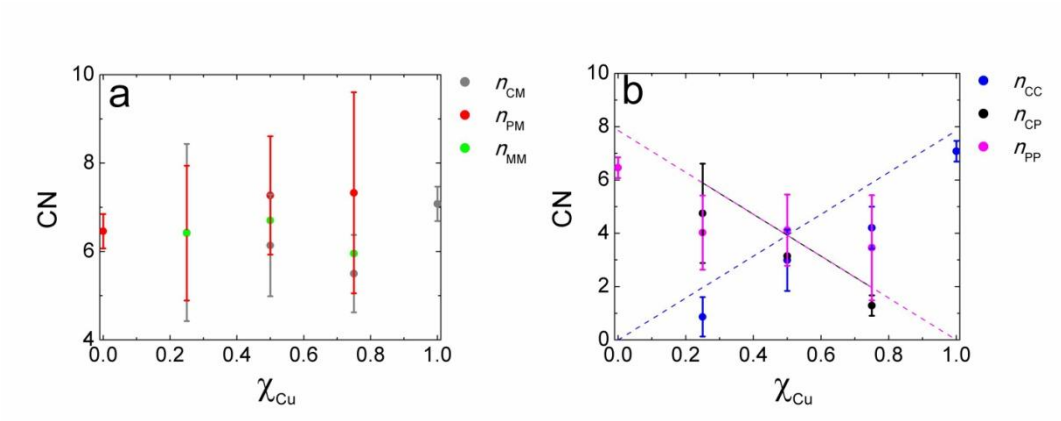

Figure 3.5.

(a) Pd-M, Cu-M, and M-M CN as a function of Cu composition. (b) Cu-Cu, Cu-Pd, and Pd-Pd coordination numbers as a function of Cu composition. The theoretical values for a 55 atom random alloy are indicated by dashed lines.

However, if the DENs were to have a true Pd-core/Cu-shell structure, n_{PdM} would be predicted to have a much higher value (>10.7) in the G6-OH($Pd_{16}Cu_{48}$) DENs. In this instance, nearly all of the 16 Pd atoms would be within the interior of the particle. Likewise, in Cu-core/Pd-shell material, n_{CuM} of the G6-OH($Pd_{48}Cu_{16}$) DENs would have a similarly high value.

The trends in the Cu-Cu CNs (n_{CuCu}) and n_{CuPd} agree very well with the ideal alloy model (Figure 3.5b). The Pd-Pd CNs (n_{PdPd})) are slightly higher, especially for the G6-OH($Pd_{16}Cu_{48}$) DENs. This difference, however, falls within the uncertainty of the fits. Accordingly, it is not possible to distinguish, in this particular case, a

completely random and homogeneous alloy from an alloy having either a Pd- or Cu-rich core.

3.4 Summary and Conclusions

The synthesis and characterization of Pd and Cu monometallic and PdCu bimetallic nanoparticles prepared within G6-OH dendrimer templates were reported. Bimetallic nanoparticles, such as those described here, are predicted by theory to have desirable catalytic properties.[82,98] UV-vis, TEM, and EXAFS data for these PdCu DENs are consistent with their size corresponding to an average of ~64 atoms. Moreover, for the bimetallic DENs, the results indicate at least partial alloying of the two metals although the degree of alloying cannot be determined.

The ability to synthesize and characterize nearly monodisperse and fully stable particles in this size regime is important to the larger goal of correlating the size, composition, and structure of DENs to their catalytic function.

Chapter 4: In-situ Structural Characterization of Platinum Dendrimer-Encapsulated Oxygen Reduction Electrocatalysts

4.1 Introduction and Background

In this chapter the structural evolution of Pt DENs containing ~225 atoms during the electrocatalytic ORR is presented. These findings are based on in-situ electrochemical EXAFS measurements, which probe the local coordination environment of the Pt electrocatalyst. There are two important outcomes of these experiments. First, the Pt CN decreases when the electrode potential is moved to positive values, which is most likely due to disordering of the Pt at the particle surface, as shown below. Furthermore, the particles show evidence of disorder at potentials in the double-layer region. Second, ligand effects on the structure of the Pt nanoparticle arising from dioxygen are minimal, although other electrolytic species may have a significant effect.

DENs are well suited for studying fundamental aspects of catalysis because of their uniform size, structure, and composition, and because the dendrimer shell prevents agglomeration without passivating the metal surface.[21,99] The small size of DENs (40-250 atoms) makes them particularly well-suited for studying catalytic reactions using in-situ EXAFS. This is because EXAFS measures the average coordination environment of a material, and small particles,

such as DENs, possess a high ratio of surface atoms to interior atoms. Therefore, interactions between the surface of the DEN and reactants and products that might influence its structure are easily observed. For larger particles, the CNs of the reactive surface atoms will be overwhelmed by the much greater signal arising from interior atoms.

There have been two previously reported in-situ electrochemical EXAFS studies of DENs.[52,100] In one case, Pt DENs containing ~240 atoms were characterized during electrochemical CO adsorption and oxidation.[100] The results indicated that CO adsorbs to the DEN surface, but that no significant degree of nanoparticle restructuring takes place before, during, or after adsorption. In the second study, the UPD of Cu onto Pt DENs was examined.[52] The core@shell structure of these materials was confirmed by analysis of the CN of each metal species. A key result of this study was that UPD layer of Cu did not affect the calculated CN of the Pt core. In other words, both of these studies indicated that ligand adsorption (CO in one case, and Cu in the other) has little or no effect on the structure of the Pt DENs. This is an important finding, because it suggests that DENs are relatively insensitive to surface processes and hence may be good experimental catalyst models for comparison to theoretical calculations.

In addition to the work with DENs, there have been a number of other in-situ EXAFS studies of Pt nanoparticles

synthesized by more traditional means.[101-113] Most of these have been focused on Pt oxide formation under steady-state conditions.[101-110] A decrease in the Pt-Pt CN (n_{PP}) and an increase in the Pt-O CN (n_{PO}) are typically observed when the electrode potential is moved from the Pt double-layer region[100] (where the ORR is active) to more positive potentials where the ORR is not active. However, one study reported no change in n_{PP} over this same potential range.[101] In general, the magnitude of the change in n_{PP} and n_{PO} is dependent on particle size, with smaller particles exhibiting greater changes in CN.[102-113] As discussed earlier, this is primarily because a higher fraction of atoms reside on the surface of smaller particles.

Recently, several groups have reported in-situ studies of proton exchange membrane fuel cells (PEMFCs) incorporating Pt nanoparticle ORR catalysts.[114-117] All of these studies utilized a two-electrode configuration incorporating a Pd anode and a cathode composed of Pt/C catalyst dispersed on a carbon support. The results obtained from these studies vary considerably and in some instances the conclusions are inconsistent.

In the present work, it was found that the effect of ligands (dioxygen species) on Pt DENs is minimal during the ORR, but that other electrolytic species may have a significant impact on DEN structure. Additionally, a reversible decrease in n_{PP} was measured as a function of

increasing potential above -0.20 V. A model of increasing surface disorder beginning at or below a potential of -0.20 V is proposed.

4.2 Experimental

DEN synthesis. G6-OH in methanol were purchased from Dendritech, Inc (Midland, MI). The methanol was removed by vacuum evaporation prior to use and a 100.0 μM aqueous stock solution was prepared from the dried powder. Sufficient 0.10 M K_2PtCl_4 (Sigma-Aldrich) was added to an aqueous solution of G6-OH so that the ratio of Pt^{2+}:G6-OH was 225:1 and the final concentration of G6-OH was 10.0 μM. This solution was allowed to react for 72 h, after which 10 molar equivalents (relative to the total metal content) of freshly prepared $NaBH_4$ were added. The resulting solution was tightly capped and allowed to react for an additional 22 h. Next, the Pt DEN solution was dialyzed into 4 L of water for 24 h using a 12.0 kDa cutoff dialysis sack (Sigma Aldrich). All aqueous solutions were prepared using 18 MΩ•cm Milli-Q water (Millipore, Bedford, MA).

DEN characterization. UV-vis absorbance spectra were collected before and after chemical reduction using a Hewlett-Packard HP8453 spectrometer and a 1.00 mm path-length quartz cuvette. A solution of 10.0 μM aqueous G6-OH was used for the blank. All spectra were consistent with previously published reports for Pt DENs of this size.[45,52]

Micrographs obtained by TEM were collected using a JOEL-2010F TEM operating at 200 kV in transmission mode. TEM grids were prepared by dropping several microliters of the DEN solution onto a carbon-coated, 400-mesh Cu grid (EM Sciences) and drying in air. The average diameter of the Pt DENs used in this study, 1.8 ± 0.3 nm, was determined by measuring 100 individual particles. This size is consistent with previously published results.[45,52,67,100]

Electrochemistry. Electrochemical experiments were performed using either GCE and a standard three-electrode cell, or a carbon-paper electrode (Avcarb75, Ballard Power Systems, Inc.) and a spectroelectrochemical cell. The counter electrode was a glassy carbon chip and the reference electrode was Hg/Hg_2SO_4. All potentials are reported relative to the Hg/Hg_2SO_4 reference electrode. High purity $LiClO_4$ (99.99%, Aldrich), $HClO_4$ (Ultrapure, JT Baker), and H_2SO_4 (Trace metal grade, Fisher) were used as supporting electrolytes. A CHI 700d bipotentiostat (CH Instruments, Austin, TX) was used for experiments carried out in the three-electrode cell. The GCE was polished sequentially with 1.0, 0.3, and 0.05 μm alumina particles, and then sonicated in water for several minutes prior to use. Details of the immobilization of the DENs onto the GCE are given in the Results and Discussion section. For in-situ EXAFS electrochemical measurements, a portable Pine WaveNow potentiostat (Pine Research Instrumentation, Grove City, PA)

was used. The carbon-paper electrode was cycled between 1.50 and -1.50 V in 0.5 M H_2SO_4 before immobilization of the DENs. Additional information about DEN immobilization onto the carbon-paper electrode is also provided in the Results and Discussion section.

Spectroelectrochemical cell. Previous publications have discussed the design of a three-electrode, in-situ, XAS cell.[52,100] A similar cell design was utilized here (Figure 4.1).

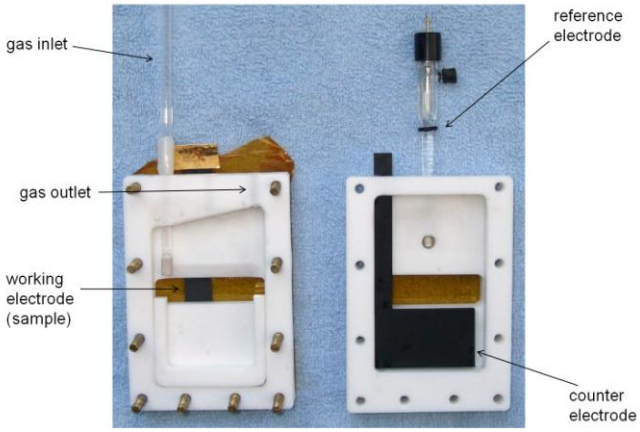

Figure 4.1.

Photograph of the spectroelectrochemical cell used for XAS studies. The cell has been disassembled for clarity. When assembled, the two halves are folded together in a manner similar to closing a book, and then the interior volume is filled with electrolyte.

Briefly, the cell consists of two Teflon pieces that are clamped together to form an electrolyte reservoir. A window in the cell allows the X-ray beam to pass through the working electrode, and Kapton tape is used to seal the

window. Ports are provided for reference and counter electrodes, as well as for gas sparging.

X-ray absorption spectroscopy. XAS data were collected using beamline X18B at NSLS at the BNL in New York (USA). The L_3 absorption edge of Pt was measured in fluorescence mode by orienting the electrode at 45° relative to the beam. A five-grid Lytle detector filled with Ar gas was used for fluorescence detection, and Soller slits and a Zn filter were used. Between 2 and 6 energy scans using 3.0 s integration times were averaged to improve the signal-to-noise ratio of the EXAFS spectra. Pt foil reference spectra were collected concurrently with the DENs spectra and used for energy calibration. The data were analyzed using the IFEFFIT software package and FEFF6 program.[87,88]

4.3 Results and Discussion

Pt DEN synthesis. Complete information about the synthesis of Pt DENs is provided in the Experimental Section, but, briefly, they are synthesized and prepared for electrocatalytic studies using the following three-step procedure. First, an appropriate, stoichiometric amount of $PtCl_4^{2-}$ is added to an aqueous dendrimer solution. This results in complexation between Pt^{2+} and tertiary amine groups present within the dendrimer interior.[45,59] Second, an excess of BH_4^- is added to the Pt^{2+}-dendrimer complex to reduce Pt^{2+} to zerovalent Pt. However, it was previously shown that reduction of Pt^{2+} is not complete under these

conditions.[45,100] Instead, a bimodal product distribution results, consisting of fully reduced nanoparticles and unreduced Pt^{2+}-dendrimer complex.[45] Third, the Pt DENs are dialyzed to remove reaction byproducts. Note that dendrimer-bound Pt^{2+} that remains unreduced after addition of BH_4^- can be fully reduced after electrode immobilization by applying a sufficiently negative electrode potential.[100]

Ex-situ characterization. The Pt DENs were characterized using UV-vis spectroscopy, TEM, and cyclic voltammetry. An absorbance spectra is shown in Figure 4.2.

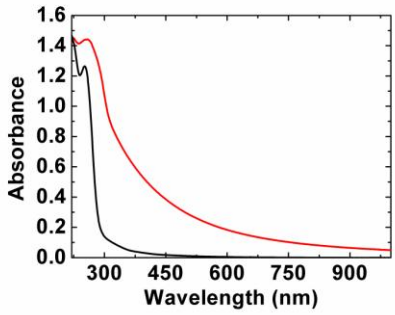

Figure 4.2.

UV-vis absorbance spectra of 10.0 µM G6-OH$(Pt^{2+})_{225}$ (black) and dialyzed G6-OH(Pt_{225}) (red). Spectra were collected using a 1.00 mm quartz cuvette. A solution containing 10.0 µM G6-OH was used for background subtraction.

A representative TEM micrograph and size-distribution histogram are shown in Figure 4.3.

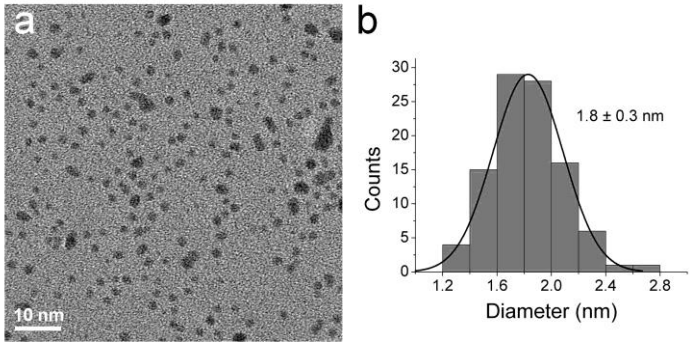

Figure 4.3.

(a) TEM micrograph and (b) particle size distribution histogram for G6-OH(Pt_{225}).

The Pt DEN system has been studied extensively, and the results obtained here are consistent with those published previously.[45,52,58,66,67,100]

The Pt DENs were characterized electrochemically using a standard three-electrode cell and a polished GCE working electrode. Immobilization of the DENs onto the GCE was achieved using a previously published method.[57] Briefly, the electrode was immersed in an aqueous solution containing 10.0 µM G6-OH(Pt_{225}) and 0.10 M $LiClO_4$, and the potential was cycled 3 times between -0.20 and 0.70 V. Next, the GCE was rinsed and transferred to a 0.10 M $HClO_4$ electrolyte solution. Finally, the electrode was cycled between 0.60 V and -0.60 V to reduce any Pt^{2+} that might be present within the dendrimers,[100] and to clean the surfaces of the DENs.

Figure 4.4 is a cyclic voltammogram (CV) of the immobilized G6-OH(Pt_{225}) DENs.

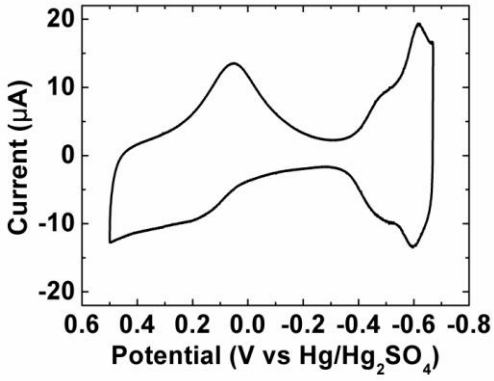

Figure 4.4.

Cyclic voltammogram obtained using a GCE modified with G6-OH(Pt_{225}) DENs. The scan rate is 100.0 mV/s, the electrode area = 7.1 mm^2, and the electrolyte solution was 0.10 M $HClO_4$ sparged with N_2.

The plot contains the characteristic features of Pt electrochemistry:[100] oxidation of Pt at potentials positive of 0.20 V, an oxide reduction peak centered at 0.10 V, and a series of peaks present at potentials negative of -0.40 V that arise from the adsorption and desorption of H atoms on different crystallographic facets of the DEN surfaces. The total surface area of Pt was determined by measuring the charge arising from hydrogen adsorption, and then converting this value to surface area using the accepted charge density value for hydrogen adsorption on bulk, polycrystalline Pt of 210 $\mu C/cm^2$.[52,67] The experimentally determined surface area (0.12 cm^2) can be compared with an estimated surface area (0.05 cm^2) calculated using assumptions discussed previously.[67] Given the approximate nature of the assumptions involved in this calculation and the conversion

of measured charge to surface area, these values are in reasonable agreement.

Immobilization of DENS onto Avcarb75. A commercial carbon-paper electrode, Avcarb75, was used as the working electrode for in-situ EXAFS measurements. Immobilization of Pt DENs onto Avcarb75 was achieved using a previously published method.[100,118] Briefly, an electrochemical pretreatment of the carbon-paper electrode in sulfuric acid was performed to improve wetting of the electrode material. A photograph illustrating this effect is provided in Figure 4.5.

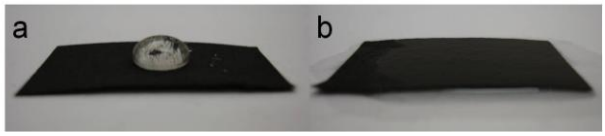

Figure 4.5.

Image of Avcarb75 carbon paper (a) before and (b) after electrochemical pretreatment using a 0.50 M H_2SO_4 electrolyte solution.

Next, the carbon paper was rinsed and immersed in a Pt DEN solution for 12 h. Finally, a CV (Figure 4.6) was obtained in the H-atom adsorption/desorption potential region to ensure the presence of G6-OH(Pt_{225}) DENs on the electrode surface.

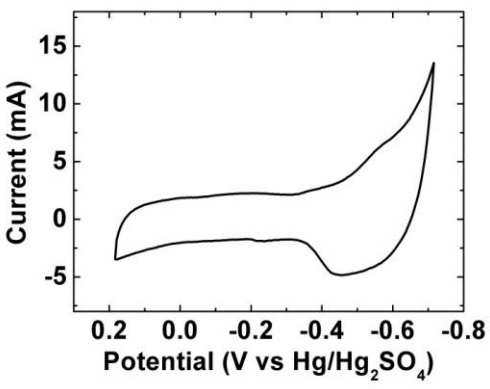

Figure 4.6.

Cyclic voltammogram obtained using an Avcarb75 carbon-paper electrode modified with G6-OH(Pt_{225}) DENs. The data were collected in a standard three-electrode cell. The scan rate is 10.0 mV/s, the electrode area = 6.5 cm^2, and the electrolyte solution was 0.10 M $HClO_4$ sparged with N_2.

Note that this CV is somewhat different from the one obtained using the GCE (Figure 4.4). This is because the surface area and resistance of Avcarb75 is greater than that of the GCE, leading to significantly increased capacitance and poorly resolved hydrogen peaks.

After trimming the Pt DEN-modified Avcarb75 working electrode and placing it into the spectroelectrochemical cell, the electrode was held at -0.70 V while sparging the electrolyte solution with N_2. As mentioned earlier, this step completes the reduction of Pt^{2+} that might be present within the dendrimers[100] and cleans the surface of the DENs. Figure 4.7 shows XANES spectra collected at the open circuit potential (OCP, black trace) before placing the working

electrode under potential control and after applying a potential of -0.70 V (red trace).

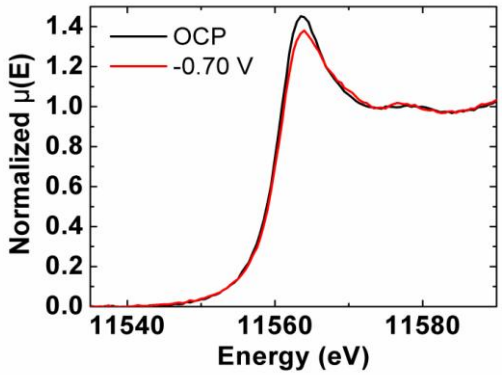

Figure 4.7.

XANES spectra of G6-OH(Pt_{225}) at the OCP and at -0.70 V collected in the spectroelectrochemical cell using 0.10 M $HClO_4$ electrolyte solution. The decrease in the white line intensity indicates reduction of Pt^{2+} after application of the negative potential.

There is a noticeable decrease in the white line region of the spectrum after application of the negative potential, indicating a lower oxidation state of Pt and hence reduction of residual intradendrimer Pt^{2+}.[108]

In-situ ORR experiments. Figure 4.8 shows CVs obtained using the spectroelectrochemical cell and a G6-OH(Pt_{225})-modified electrode in the presence (red) and absence (black) of O_2.

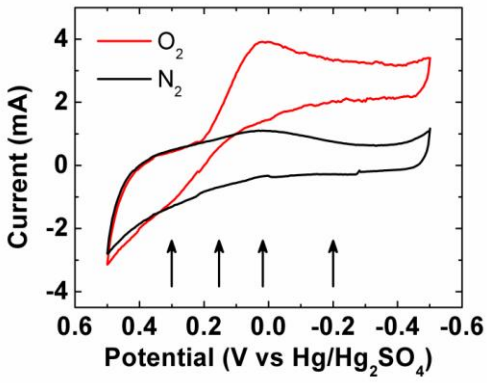

Figure 4.8.

Cyclic voltammograms obtained using an Avcarb75 carbon-paper electrode modified with G6-OH(Pt_{225}) DENs. The arrows indicate the potentials at which XAS spectra were collected. Both the voltammograms and XAS data were obtained using the spectroelectrochemical cell shown in Figure 4.1. The scan rate is 10.0 mV/s, the electrode area = 3.6 cm^2, and the electrolyte solution was 0.10 M $HClO_4$ sparged with O_2 or N_2, as indicated in the legend.

The arrows in Figure 4.8 indicate the potentials at which EXAFS spectra were collected: -0.20, 0.05, 0.15, and 0.30 V. Note that the currents in these CVs are lower than in the CV shown in Figure 4.6. This is because the area of the Avcarb75 electrode was reduced in size before placing it into the spectroelectrochemical cell.

EXAFS were data collected with the working electrode held at the desired potential while the electrolyte was sparged with either N_2 or O_2. In some cases the electrode was held at a particular potential for several hours so that multiple EXAFS scans could be collected to improve the signal-to-noise ratio of the spectra. Figure 4.9 is a plot

of current vs. time for each of the four potentials indicated in Figure 4.8.

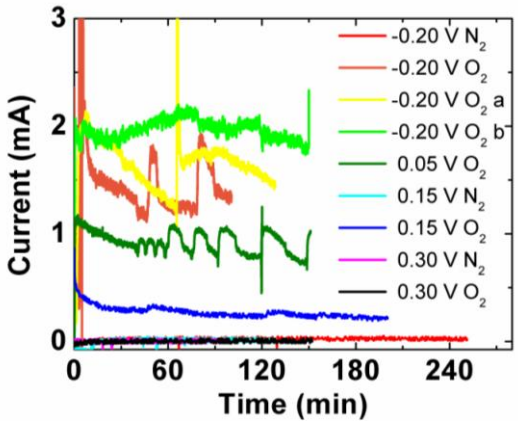

Figure 4.9.

Plots of current vs. time obtained while the G6-OH(Pt_{225})-modified Avcarb75 electrode was held under electrochemical control at the potentials indicated in the legend. Data collection was initiated (t = 0) as soon as the potential was applied, and EXAFS data collection began at t = 30 min. The 0.10 M $HClO_4$ electrolyte solution was sparged with O_2 or N_2, as indicated in the legend. The electrode area was 1.6 cm^2.

Current data collection began immediately upon application of the indicated electrode potential (t = 0) and XAS data collection began at t = 30 min (to ensure steady-state conditions). Fluctuations in the currents, which are most apparent in the dark green trace, are most likely due to bubble formation or irregular convection patterns in the cell caused by slight changes in gas flow.

In-situ XAS. The black EXAFS spectrum in Figure 4.10 was collected while the DEN-modified electrode was held at 0.15 V in 0.10 M $HClO_4$ sparged with O_2.

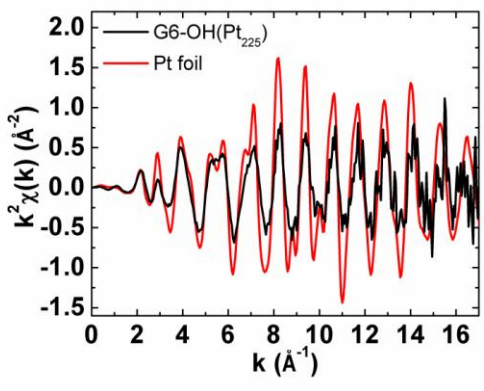

Figure 4.10.

The black trace is a representative EXAFS spectrum (Pt L_3 edge) obtained from a G6-OH(Pt_{225})-modified Avcarb75 electrode held at a potential of 0.15 V in 0.10 M $HClO_4$ sparged with O_2. The red trace is a spectrum of a Pt foil. EXAFS spectra obtained under other conditions are provided in Figure 4.11.

The red spectrum was obtained from a Pt foil collected on the same beamline. EXAFS spectra obtained under other conditions are provided in Figure 4.11.

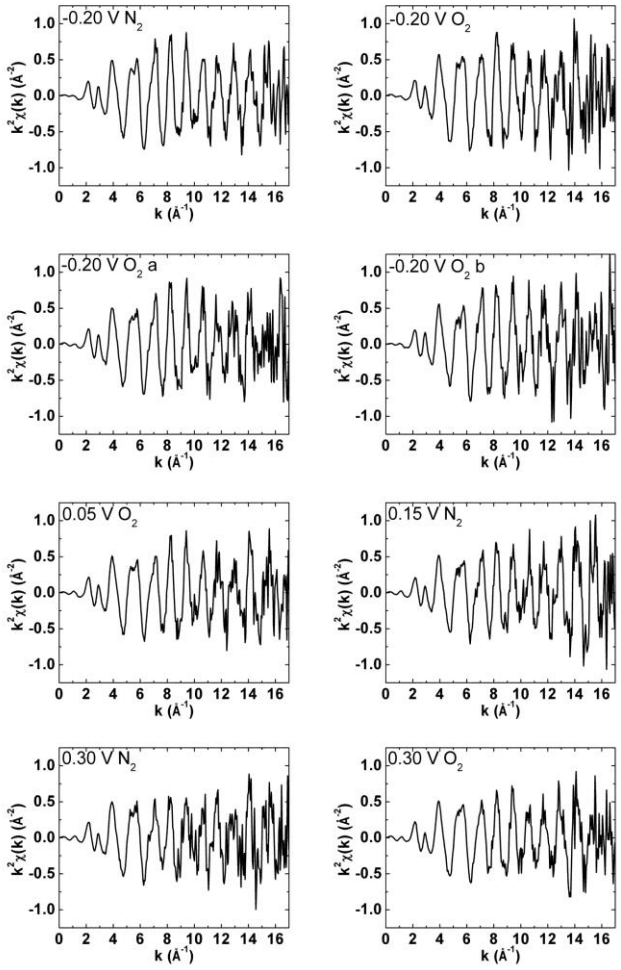

Figure 4.11.

EXAFS spectra of the Pt L_3 edge of G6-OH(Pt_{225}) maintained at the indicated potentials in the spectroelectrochemical cell while sparging with N_2 or O_2.

All spectra exhibit decreased amplitudes relative to the bulk Pt, which is characteristic of nanoparticles.[96] The data were fit using *k* windows that began at 3 $Å^{-1}$ and extended to values between 12 and 15 $Å^{-1}$, depending on the noise present in each spectrum at high *k*. For example, the

data shown in Figure 4.6 was fit from k = 3 - 12.5 Å^{-1}. The complete set of k windows used to fit all the EXAFS spectra, along with the R_{bkg} and R window values, are provided in the Table 4.1.

Fitting parameters used for the EXAFS simulations.

	k_{min} (Å^{-1})	k_{max} (Å^{-1})	R_{min} (Å)	R_{max} (Å)	R_{bkg} (Å)
-0.20 V N_2	3	14.0	1.30	3.30	1.3
-0.20 V O_2	3	12.0	1.35	3.15	1.3
0.05 V O_2	3	12.5	1.50	3.10	1.3
0.15 V O_2	3	12.5	1.50	3.10	1.3
0.15 V N_2	3	12.0	1.40	3.30	1.3
-0.20 V O_2	3	12.0	1.40	3.15	1.3
0.30 V O_2	3	13.0	1.45	3.10	1.3
0.30 V N_2	3	12.0	1.50	3.30	1.3
-0.20 V O_2	3	15.0	1.40	3.30	1.3

Table 4.1.

To eliminate multiple-scattering effects and minimize the number of variables in the fit model, only the first Pt-Pt and Pt-O coordination shells were used for each spectrum. The best model was chosen on a sample-by-sample basis, as determined by the statistical fit parameters and by visual agreement of the experimental spectra and fit results. A multiple-scattering analysis of the sample at -0.20 V with N_2 sparging was also performed, as discussed in the following section.

Figure 4.12 is a histogram showing the Pt-Pt and Pt-O CNs (n_{PP} (black) and n_{PO} (red), respectively) for each experiment.

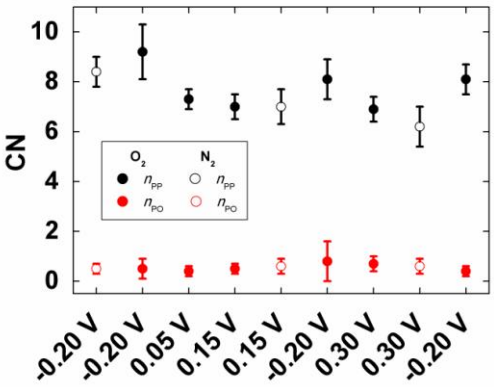

Figure 4.12.

Pt-Pt (n_{PP}) and Pt-O (n_{PO}) coordination numbers, determined from fits to the EXAFS data, as a function of electrode potential for G6-OH(Pt_{225}) DENs. Data were obtained using a 0.10 M $HClO_4$ electrolyte solution sparged with either N_2 or O_2. The potentials are given in the order of data collection.

CNs determined for Pt DENs in the presence of O_2 and N_2 are represented by filled and empty circles, respectively. The data are plotted in the order collected, beginning with the most reducing potential (-0.20 V) and continuing to the most positive potential (0.30 V). Several replicate data points were collected at -0.20 V under O_2 sparging to ensure that differences in CNs arise from electrode potential changes rather than drift or other irreversible effects. The results in Figure 4.12 as well as the values obtained for

the other fitting parameters are presented in numerical form in Table 4.2.

Fit values obtained from EXAFS simulations.

	O_2					
Potential (V)	0.3	0.15	0.05		-0.2	
n_{PP}	6.9(5)	7.0(5)	7.3(4)	9.2(1.1)	8.1(8)	8.1(6)
n_{PO}	0.7(3)	0.5(2)	0.4(2)	0.5(4)	0.8(8)	0.4(2)
R_{PP} (Å)	2.751(4)	2.745(4)	2.734(3)	2.745(7)	2.747(6)	2.740(3)
σ^2_{PP} (Å^2)	0.0064(5)	0.0060(5)	0.0062(4)	0.0067(8)	0.0060(7)	0.0058(3)
R_{PO} (Å)	0.017(14)	0.019(15)	0.009(14)	0.015(33)	0.025(38)	0.010(17)
σ^2_{PO} (Å^2)	0.003(4)	0.001(4)	0.001(4)	0.003(9)	0.011(15)	0.000(3)
ΔE_0 (eV)	8.6(8)	8.0(8)	7.6(6)	8.5(1.2)	8.4(1.1)	7.1(7)

	N_2					
Potential (V)	0.3	0.15			-0.2	
n_{PP}	6.2(8)	7.0(7)			8.4(6)	
n_{PO}	0.6(3)	0.6(3)			0.5(2)	
R_{PP} (Å)	2.752(7)	2.748(5)			2.747(3)	
σ^2_{PP} (Å^2)	0.0062(4)	0.0064(6)			0.0066(9)	
R_{PO} (Å)	-0.006(16)	0.021(19)			0.055(16)	
σ^2_{PO} (Å^2)	0.000(3)	0.003(5)			0.000(4)	
ΔE_0 (eV)	8.6(7)	8.2(7)			7.9(1.2)	

Table 4.2.

Several observations can be drawn from Figure 4.12. First, there is a significant increase in n_{PP} at more negative potentials in the presence of both O_2 and N_2. At -0.20 V, the most reducing potential considered in this study, n_{PP} is between 8 and 9.2. This is somewhat lower than the theoretical n_{PP} (9.5) for a 225-atom fcc truncated octahedral particle. However, when multiple-scattering analysis and electron microscopy measurements are taken into account, the EXAFS results are consistent with the nominal 225-atom clusters (vide infra). Previous studies with Pt DENs demonstrated n_{PP} greater than or equal to the predicted values at an even more reducing potential (-0.70 V) under similar conditions.[100] This is consistent with the trend observed here for the CN to increase at more negative potentials. Second, there is no significant difference between n_{PP} and n_{PO} collected in the presence of O_2 and the N_2. However, as indicated in Table 4.2, there may be a systematic effect of increased Pt-Pt bond lengths (R_{PP}) under N_2 sparging. Finally, the changes in the coordination environments of the particles under potential control appear to be largely reversible (compare the values of n_{PP} at -0.20 V in Table 4.2).

Multiple-scattering analysis. Previous studies have shown that the CNs of multiple-scattering contributions to EXAFS data in small nanoparticles can be used to distinguish between different particle geometries.[95,96,119-121] A multiple-

scattering fit of the EXAFS spectra collected while the DENs were held under the most reducing potential (-0.20 V) was performed to characterize the size and shape of the particles. Figure 4.13 shows the Fourier-transformed EXAFS spectra and the multiple-scattering analysis of the Pt DENs measured at -0.20 V while sparging with N_2.

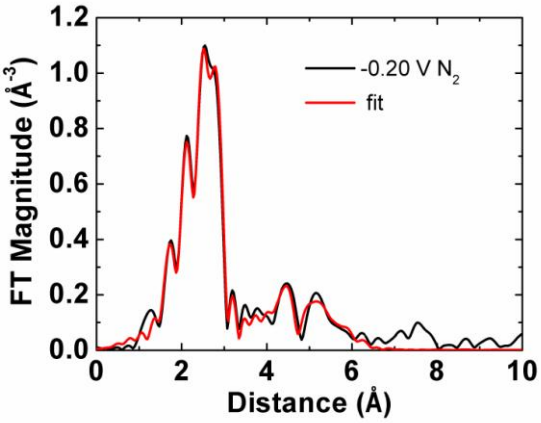

Figure 4.13.

Fourier transformed EXAFS spectrum obtained from (black trace) a G6-OH(Pt_{225})-modified Avcarb75 electrode held at a potential of -0.20 V in 0.10 M $HClO_4$ sparged with N_2. The red trace is the multiple-scattering fit to these data. The k and R windows for this analysis were 2.5 - 14 and 1.30 – 6.31, respectively, and R_{bkg} = 1.3.

Table 4.3 compares the predicted CNs of the first four coordination shells (N1 – N4) for several types of fcc clusters to the values obtained from the multiple-scattering fit.

Coordination numbers for fcc cluster models and experimental results for multiple-scattering fit analysis of the data collected at -0.20 V under N2 sparging.

	140 atoms D=1.5 nm	147 atoms D=1.7 nm	225 atoms D=2.0 nm	Experiment D=1.8(3) nm
		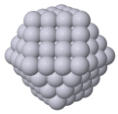		
N1	9.1	9.0	9.5	8.4(4)
N2	3.6	4.0	3.8	3.3(2.3)
N3	13.4	13.1	14.7	20.1(7.7)
N4	6.2	6.1	7.0	6.0(2.3)
NO	--	--	--	0.4(1)

Table 4.3.

The effective diameters of the clusters and the average diameter of the particles (as determined by TEM) are also included in the table. The experimental CNs and TEM data are consistent with a model of small, quasi-spherical clusters, although the observed first nearest neighbor (1NN) CNs are smaller than the model values. Further discussion of this observation is given below. Interpretation of the multiple-scattering fit analysis for Pt DENs held at potentials greater than -0.20 V is more complicated due to larger number of possible models, and therefore this discussion is limited to this single potential.

Analysis of the results. Guided by the combination of the in-situ EXAFS results and the ex-situ TEM data, the most

plausible scheme for structural transformations that occur in the Pt DENs at different potentials will be discussed. Several possible scenarios and how they compare with relevant data will be reviewed.

Certain models are consistent with the observation of a decreasing n_{PP} with increasing potential and, yet, should be discounted as inconsistent with other information about the system. For instance, dissolution of the Pt atoms from the particles will result in smaller nanoparticles and free, uncoordinated (or, alternatively, polymer- or oxygen- or hydroxocomplex-bound) Pt atoms or ions, thereby lowering n_{PP}.[55] However, such dissolution would likely result in irreversible changes to n_{PP}. Additionally, the reduction of n_{PP} caused by dissolution should be accompanied by even greater reduction in the contribution from the higher-order coordination shells. Indeed, let us assume for simplicity that all 225-atom clusters decomposed into identical small particles with CNs between 6 and 7 (Table 4.2). These CNs correspond to the closed shell clusters of ~13 atoms (considering either close-packed fcc or non-close-packed icosahedral clusters).[119] In such clusters, the EXAFS signal originating from higher-order shells will be transparent to EXAFS.[122] Figure 4.14 plots selected Fourier-transformed EXAFS spectra.

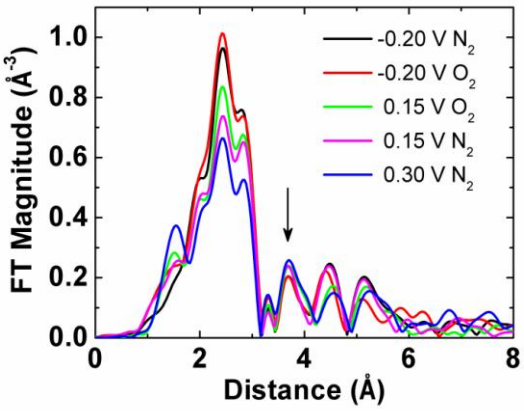

Figure 4.14.

Fourier transformed EXAFS spectra. All data shown have an R_{bkg} of 1.3 and a k-range of 3 – 12.

The peak marked with the arrow corresponds primarily to second-shell coordination, and the peaks at higher R are due to correspondingly higher coordination shells. Their presence rules out decomposition of the nanoparticles into smaller clusters.

Another possible explanation for a decrease in n_{PP} with increasing potential is the formation of surface oxides.[110] Oxidation of the surface will reduce the CN in two ways. First, if PtO_n forms on the surface of the particles, it may disrupt Pt-Pt metal bonding thereby lowering the ensemble-average CN for Pt metal. Second, recent studies have shown that increased asymmetric disorder (caused by, for example, ligand-induced strain)[123] in nanoparticles relative to bulk materials leads to decreased apparent metal CNs in the nanoparticle systems.[124] Accordingly, it would be possible

for adsorption of electrochemically produced ligands to disrupt the first Pt shell without affecting the ordered metal core. These species could include electrogenerated oxygenated Pt intermediates,[110] which could be present even in the absence of O_2 (this is, under N_2 sparging conditions). Such disorder is inherently asymmetric and can lead to the apparent reduction in CN described above. As the surface disorder increases at increasingly higher potentials, the signal from higher order shells will become progressively less and less intense. Although a clear trend of decreasing multiple-scattering signal is not observed, the data are consistent with a model of increasing disorder at the higher potentials (Figure 4.14).

Given the discussion thus far, an "ordered core-disordered shell" model is proposed. This model assumes that the nanoparticle surface is already partially disordered even at -0.20 V, and that it becomes further disordered as oxidation of Pt begins to occur. However, in this model, the Pt core remains relatively ordered at all potentials. The fact that the shell is always disordered explains why multiple-scattering contributions are relatively unaffected by changes to the electrode potential. Indeed, multiple-scattering contributions in an fcc structure are dominated by collinear Pt-Pt-Pt arrangements, and they decrease in proportion to the square of the bonding angle when bonding disorder is present.[125,126] Therefore, a

large signal intensity in the high R-region, and, hence, the multiple-scattering contributions, should be dominated by the ordered core in such systems even for small angular disorder. Therefore, even as disorder increases, there is little additional effect on the multiple-scattering contribution. This model is supported by the multiple-scattering analysis described in the previous section (Table 4.3). Smaller-than-predicted CNs are observed for most shells at -0.20 V, although the diameter of the 225-atom, truncated octahedron model agrees with the TEM. This suggests the presence of disorder in the outermost DEN shell even at this potential.

It is important to mention that although this study provides evidence for surface disorder at potentials > -0.20 V, at even more reducing potentials the particles are clearly faceted. This is apparent from the well-defined hydrogen atom adsorption/desorption peaks present in Figure 4.4 at potentials <-0.4 V. This observation is fully consistent with the model described above, and it clearly shows that even in DENs, which are not in direct contact with the electrode surface, the electrode potential has a significant influence on particle structure.

4.4 Summary and Conclusions

DENs are good model systems for studying catalytic processes using EXAFS because of their well-defined structural properties and high proportion of surface atoms

relative to fully coordinated atoms. That is, because ~65% of the atoms in a G6-OH(Pt_{225}) particle are predicted to be at the surface, the effects of reaction intermediates on the surface atoms of DENs are observable in EXAFS.

The principal finding to emerge from the present study is that the Pt-Pt CN is a function of the electrode potential. This result may be interpreted in terms of a model in which only the outermost Pt shell is affected by the potential. Specifically, at strongly reducing potentials (<-0.4 V) the outer Pt shell is order, as evidenced by the presence of well-defined H-atom adsorption and desorption peaks in the voltammetry. However, as the potential is moved positive, into and past the double-layer potential region, increasing disorder is signaled by a reduction in the Pt-Pt CN observed by in-situ EXAFS experiments. Such order/disorder transitions are likely to have a dramatic effect on electrocatalytic reactions, and therefore this type of behavior is an interesting focus for future studies.

One final point is worth mentioning. There is a fundamental difference between DENs and all other Pt nanoparticle systems that have been examined by EXAFS previously. Specifically, in the case of DENs, the nanoparticle is not in direct contact with the electrode surface. Rather, it is sequestered within the dendrimer a small distance away. Therefore, DENs provide a good model

system for studying the effects of adsorbates and electrode potential in the absence of specific interactions exerted by the electrode surface. In other cases, substrate effects tend to have a strong influence on nanoparticle structure, and smaller effects driven by adsorbates or potential may be swamped out.

Chapter 5: Electrochemical Oxidation of Cu Dendrimer-Encapsulated Nanoparticles

5.1 Introduction and Background

In this chapter the electrochemical dissolution of Cu DENs is presented. The key finding is that there is a large, positive shift of the stripping potential caused by the interaction between the Cu and the dendrimer, but there are no size-dependent changes to the anodic stripping peak position, even relative to larger DSN structures. This study is significant because it probes the stability of small (<1.5 nm), unsupported Cu nanoparticles.

In addition to stabilizing the encapsulated nanoparticle, the dendrimer can be used as a handle for attaching a DEN to a substrate, such as an electrode.[57] Because the dendrimer is only weakly associated with the nanoparticle surface,[21,67,127] DENs are excellent models for studying the electrochemical properties of nanoparticles of <250 atoms.[11,52,53,57,67,100] For instance, size-dependent effects on the ORR of Pt DENs[67] has been observed and facet-selective UPD of Cu onto Pt DENs has been demonstrated.[52]

The size-dependent stability of nanoparticles to electrochemical oxidation was first investigated in 1982 when Plieth predicted small particles to be less stable against oxidation with an inverse dependence between E^0 and the radius of the nanoparticle.[128] This effect is a result of the increased surface energy of nanoparticles relative to

a bulk sample and has important consequences for industrial applications where the long-term stability of nanoparticle catalysts may be required.[129] There have been several size-dependent anodic stripping voltammetry (ASV) studies that have corroborated Plieth's prediction.[129-131] However, there have also been reports of increased stability of very small Ag[132] and Cu[133] nanoparticles against oxidation.

Subnanometer diameter Ag clusters deposited on highly oriented pyrolytic graphite (HOPG) were found to persist for up to an hour at potentials +500 mV of the Ag^0/Ag^+ Nernst potential.[132] In another study, Cu clusters of <100 atoms were deposited on a Au substrate.[133] The small clusters were stable for ~1 h at a potential +10 mV of the Cu^0/Cu^{2+} Nernst potential. At +100 mV, the particles underwent a slow, layer-by-layer dissolution, with each atomic layer displaying increased resistance to oxidation (slower dissolution). In contrast to the present study, the Ag and Cu nanoparticles described above were located directly on a substrate support.

In another study relevant to this work, Berchmans et al. complexed Cu^{2+} to a G4 PAMAM dendrimer film on a Au electrode, and used electrochemical reduction to produce nanoparticles of ~100 nm in diameter.[134] The authors also used the dendrimer film to preconcentrate Cu^{2+} ions at pM concentrations for detection by ASV.

In the present paper, Cu DENs containing ~16-55 atoms were drop-cast onto a GCE and ASV was used to investigate the electrochemical dissolution of the nanoparticles. This behavior was also compared to that of Cu DSNs. As discussed previously, DSNs are not located within the voids of a single dendrimer, but consist of a nanoparticle stabilized by the peripheral groups of one or more dendrimers. A positive shift of the anodic stripping wave for Cu DENs and DSNs of ~+400 mV relative to the stripping wave of free, reduced Cu salt occurs. Additionally, no size-dependent effects on the stripping wave were observed.

5.2 Experimental

DEN Preparation. G6-OH in methanol was purchased from Dendritech, Inc (Midland, MI). The methanol was removed by vacuum evaporation prior to use and a 50.0 μM aqueous stock solution was prepared from the dried powder. Sufficient 0.010 M $CuSO_4$ (Fisher) was added to an aqueous solution of G6-OH to yield the desired Cu^{2+}:G6-OH ratio and so that the final concentration of the dendrimer is 2.0 μM. The pH was adjusted to >10 using a solution of 1 M NaOH (EMD Chemicals, Gibbstown, NJ). Immediately before electrode preparation, a 1.0 mL aliquot of the metal-ion-dendrimer complex was reduced with 4.0 μL of freshly prepared 1 M BH_4^- (Sigma-Aldrich) and sealed for 5 min before drop-casting onto a GCE. Details for the synthesis of Pd and PdCu DENs are

given in Chapter 3. All aqueous solutions were prepared using 18 MΩ•cm Milli-Q water (Millipore, Bedford, MA).

Electrochemistry. Electrochemical experiments were performed using 3.0 mm diameter GCE, a glassy carbon chip counter electrode, and a Hg/Hg_2SO_4 reference electrode. All potentials are reported relative to the Hg/Hg_2SO_4 reference electrode. High purity $HClO_4$ (Ultrapure, JT Baker) was used for supporting electrolyte. The potentiostat used was a CHI 700d bipotentiostat (CH Instruments, Austin, TX).

The GCE was polished sequentially with 1.0 and 0.05 μm alumina particles, and then sonicated in water for several minutes and dried with N_2 prior to use. The desired volume (between 0.10-5.0 μL) of Cu DENs was drop-cast onto the electrode and dried in air or under gently streaming N_2. The electrode was inserted into a 0.10 M $HClO_4$ electrolyte sparged with Ar and immediately put under potential control at -0.50 V or -0.80 V. The electrode was then scanned from -0.50 V or -0.80 V, respectively, to 0.10 V at scan rates from 2.0-25.0 mV/s. Ar gas was continuously streamed over the top of the electrolyte solution throughout the experiment to prevent O_2 from diffusing into the solution.

5.3 Results and Discussion

Stripping voltammetry. Figure 5.1 plots the anodic stripping wave of a solution of a 110.0 μM $CuSO_4$ (no

dendrimer present) which was reduced and drop-cast onto a GCE according to the method described above.

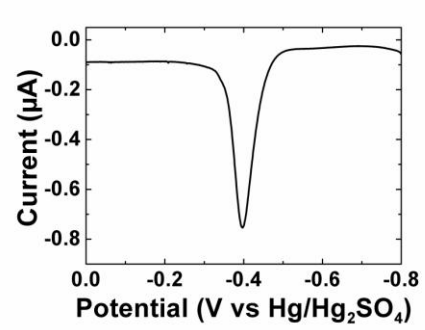

Figure 5.1.

Anodic stripping wave of reduced $CuSO_4$ in the absence of dendrimer. The electrode was prepared by reducing 1.0 mL of a 110.0 µM solution of $CuSO_4$ with 4.0 µL of freshly prepared 1 M BH_4^- and sealing for five minutes. 1.00 µL of the reduced Cu solution was then drop-cast onto a GCE and dried under blowing N_2. The scans were collected in 0.10 M $HClO_4$ at a scan rate of 5.0 mV/s.

There is a single stripping wave with a peak potential, E_p, at -0.40 V, corresponding to the oxidation of zerovalent Cu to Cu^{2+}.

When the dendrimer-metal ion complex (G6-OH$(Cu^{2+})_{55}$) is drop-cast onto the electrode prior to chemical reduction of the Cu^{2+}, a single peak is also observed at -0.39 V (Figure 5.2).

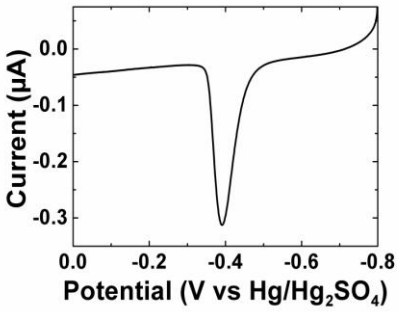

Figure 5.2.

Anodic stripping wave of G6-OH$(Cu^{2+})_{55}$. The scans were collected in 0.10 M $HClO_4$ at a scan rate of 5.0 mV/s. The electrode was prepared by dropping 1.00 μL of a 2.0 μM Cu^{2+}:dendrimer DEN-precursor solution onto a GCE and drying under blowing N_2.

The similarity of the peak potentials between the reduced, free Cu species and the metal-ion-dendrimer complex indicate that bulk-like deposition of the Cu directly onto the electrode from G6-OH$(Cu^{2+})_{55}$ likely occurs. In fact, when the electrode is maintained at potentials below -0.50 V, no stripping wave is observed for drop-cast metal-ion-dendrimer complex (Figure 5.3).

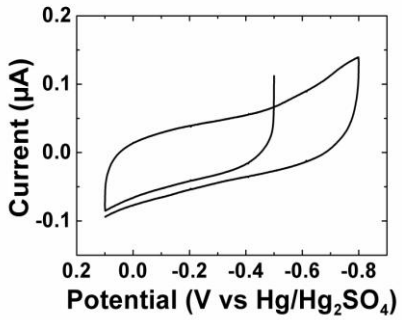

Figure 5.3.

Anodic stripping wave of G6-OH(Cu^{2+})$_{55}$. The scans were collected in 0.10 M $HClO_4$ at a scan rate of 5.0 mV/s. The electrode was prepared by dropping 1.00 µL of a 2.0 µM Cu^{2+}:dendrimer DEN-precursor solution onto a GCE and drying under blowing N_2.

This indicates that no zerovalent Cu is formed during the drying process and that electrochemical reduction of the Cu^{2+} occurs at potentials below -0.50 V.

Figure 5.4 plots the anodic stripping wave of a 2.0 µM G6-OH(Cu_{55}) sample.

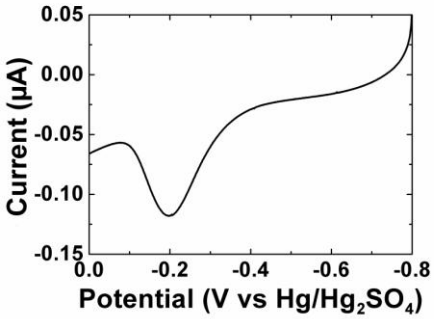

Figure 5.4.

Anodic stripping wave of G6-OH(Cu_{55}). The electrode was prepared by dropping 1.00 µL of a freshly reduced 2.0 µM Cu DEN solution onto a GCE and drying under blowing N_2. The scans were collected in 0.10 M $HClO_4$ at a scan rate of 5.0 mV/s.

Again, there is a single stripping wave corresponding to the oxidation of zerovalent Cu. However, E_p has been shifted negative to -0.20 V, indicating that the DEN is harder to oxidize than the reduced, free Cu salt. Note also that although the same mass of Cu was dropped on the GCE in Figures 5.1 and 5.4, the current is almost 10x smaller when the DENs were drop-cast to the electrode. There are two possible causes for this effect. 1) The DEN film is not stable against dissolution into the electrolyte, and the majority of the DENs diffuse away from the electrode before oxidation of the Cu. 2) The DEN film is sufficiently thick such that only a fraction of the nanoparticles are in electrical contact with the electrode. Both of these models are discussed in further detail below.

Stability of Cu DENs during immobilization. Typically, DENs are immobilized to a GCE by immersing the electrode in a solution of DENs and sweeping to potentials at or above 0.6 V.[52,57,67] Cu is not stable at these potentials and, therefore, Cu DENs cannot be immobilized to an electrode by the standard immobilization method. The Cu DENs in this study were immobilized to the electrode using a drop-casting method. Briefly, a freshly prepared Cu DEN solution is dropped onto a polished GCE and dried under air and flowing N_2 to produce a uniform film. Further details of this process are given in the Experimental section.

To test the stability of the DENs during the drying process, the DENs were dried in a H_2 atmosphere, to prevent any possible oxidation of the Cu particles.[1,51] The Cu anodic stripping wave was observed to remain unchanged when the electrodes were dried under H_2 compared to when they are rapidly dried in air (Figure 5.5).

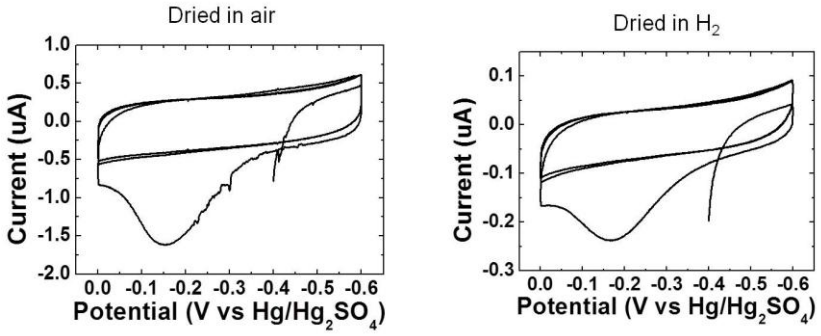

Figure 5.5.

Anodic stripping wave of G6-OH(Cu_{64}) immobilized onto vulcan carbon and dried in (left) air and (right) a H_2 atmosphere. The scans were collected in 0.10 M $HClO_4$ at a scan rate of 10.0 mV/s. The samples were prepared by reducing 1.0 mL of 2.0 µM DENs with 20.0 µL of freshly prepared 1 M BH_4^-. 2 mg of Vulcan carbon and 0.2 mL isopropyl alcohol were added and the samples were sonicated for 30 min before drop-casting 3.0 µL onto a polished GCE.

Presumably, excess, unreacted BH_4^- in the DEN solution present after reduction of the DEN precursor remains throughout the drying process, even under normal atmosphere, allowing the Cu particles to maintain their zerovalent state.

To further test this theory, a prepared electrode was allowed to sit under air for 7 h before collection of the anodic stripping wave (Figure 5.6).

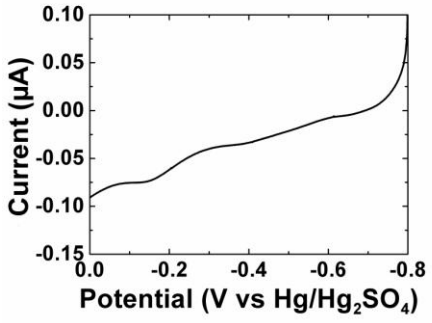

Figure 5.6.

Voltammogram of G6-OH(Cu_{55}) after prolonged exposure to air. The electrode was prepared by dropping 1.00 µL of a freshly reduced 2.0 µM Cu DEN solution onto a GCE. The electrodes were left under air for 7 h to allow any excess BH_4^- from the synthesis to react with O_2. The scans were collected in 0.10 M $HClO_4$ at a scan rate of 5.0 mV/s.

After aging, the well-defined anodic stripping wave is no longer present. Instead there are three, poorly-defined waves at ~-0.7, -0.4, and -0.2 V. This indicates that the Cu DEN films do not remain stable with prolonged exposure to air.

Additional evidence that the BH_4^- remains throughout the drying process is provided by a study of drop-cast PdCu DENs. Figure 5.7 shows a voltammogram of a PdCu DEN film.

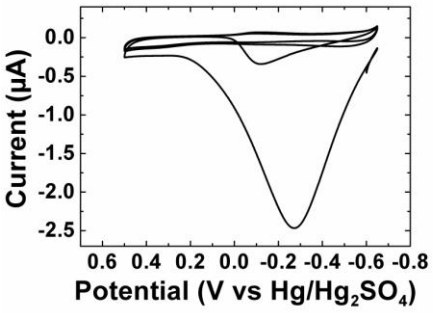

Figure 5.7.

Voltammogram of G6-OH($Pd_{64}Cu_{48}$) drop-cast and dried in a N_2 atmosphere. The sample was prepared by reducing 5.0 mL of a 2.0 μM PdCu DEN solution with 20.0 μL of freshly prepared BH_4^-. 3.0 μL of the DENs were drop-cast onto a GCE and dried for several minutes under N_2. The voltammogram was collected 5 min after inserting the GCE into the electrochemical cell. The scans were collected in 0.10 M $HClO_4$ at a scan rate of 5.0 mV/s.

Excess BH_4^- trapped in the DEN film produces H_2 upon reaction with the water. Because PdCu DENs are catalysts for H_2 oxidation, there is a large anodic current at potentials where Pd metal is present. (This effect is also observed for Pd DEN drop-cast films.) After cycling several times, the current due to H_2 oxidation disappears, indicating all of the BH_4^- has been removed from the system.

A Pd DEN film was prepared on an electrode and held at reducing potentials for 30 min in acidic electrolyte before ASV (Figure 5.8).

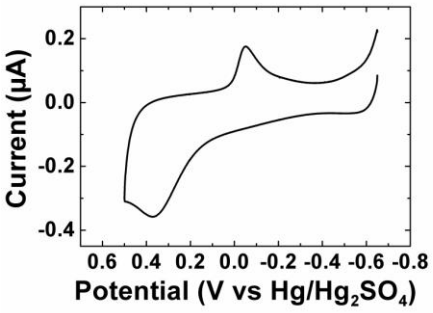

Figure 5.8.

Voltammogram of G6-OH(Pd_{128}) after being held under potential control for 30 min. 20.0 μL of freshly reduced 1 M BH_4^- solution was added to a 1.0 mL aliquot of a 2.0 μM Pd DEN solution and sealed for 5 min. 1.00 μL of the reduced DENs were drop-cast onto a GCE and dried under gently blowing N_2. The electrodes were inserted into the electrochemical cell and held at -0.5 V for 30 min. The scans were collected in 0.10 M $HClO_4$ at a scan rate of 5.0 mV/s.

No H_2 oxidation wave is observed, indicating this method is sufficient to remove any BH_4^- from the system. Figure 5.9 shows the anodic stripping of a Cu DEN sample that was held at reducing potentials for 30 min.

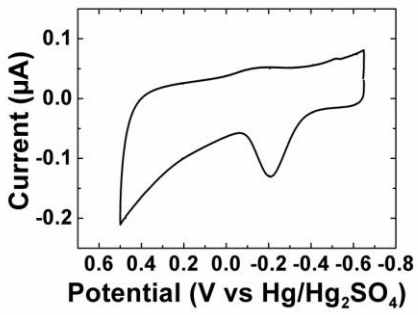

Figure 5.9.

Voltammogram of G6-OH(Cu_{64}) after being held under potential control for 30 min. 20.0 μL of freshly reduced 1 M BH_4^- solution was added to a 1.0 mL aliquot of a 2.0 μM Cu DEN solution and sealed for 5 min. 1.00 μL of the reduced DENs were drop-cast onto a GCE and dried under gently blowing N_2. The electrodes were inserted into the electrochemical cell and held at -0.5 V for 30 min. The scans were collected in 0.10 M $HClO_4$ at a scan rate of 5.0 mV/s.

Under these conditions, E_p remains shifted out to -0.20 V. This indicates the shift in the Cu stripping peak is not caused by BH_4^-.

Scan rate and loading dependence. Figure 5.10a plots the anodic stripping wave of G6-OH(Cu_{55}) at several scan rates, ν, from 2.0–25.0 mV/s.

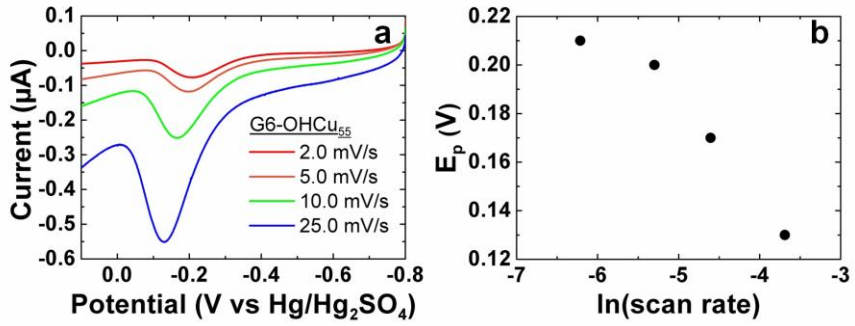

Figure 5.10.

(a) Voltammogram illustrating the effect of scan rate on the Cu stripping waves of G6-OH(Cu_{55}) immobilized onto a GCE. The electrodes were prepared by dropping 1.00 μL of a freshly reduced 2.0 μM Cu DEN solution onto a GCE and drying under blowing N_2. The scans were collected in 0.10 M $HClO_4$ at scan rates from 2.0-25.0 mV/s. (b) Dependence of E_p on the ln(ν). A linear dependence is observed for scan rates at or above 5.0 mV/s.

The peak position, E_p, is observed to shift positive proportionally to ln(ν) (Figure 5.10a), at scan rates at or above 5.0 mV/s. This matches a prediction of a linear dependence of E_p on scan rate for particle dissolution from electrode surfaces made by Compton and coworkers.[135] These predictions are based on models that do not take into account nanoparticle size effects (such as a shift in E^0), but are based on the mass transport of metal to and from the electrode.

One disadvantage of the drop-casting immobilization method is the difficulty in producing even, monolayer coverage over the electrode surface. For instance, assuming an immobilized dendrimer footprint of 7.0 nm in diameter for

G6-OH PAMAM dendrimer on the electrode surface and a roughness factor of 2.4[67] for the GCE, monolayer coverage on a 3.0 mm disk electrode would require even deposition of 0.73 pmol of DENs. While it is possible to reproducibly measure this quantity of DENs, producing a uniform film at monolayer thickness is practically unfeasible. It was found that a much more uniform film was obtained with higher electrode loadings.

The Cu loading on the electrode was varied by drop-casting differing volumes of a 2.0 µM G6-OH(Cu_{55}) solution onto the GCE. E_p is observed to be nearly constant at lower Cu coverages, but shifts to more positive values at higher loading (Figure 5.11a).

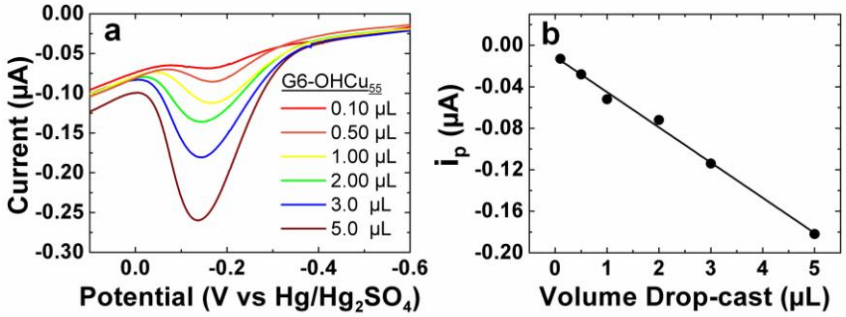

Figure 5.11.

(a) Anodic stripping wave of G6-OH(Cu_{55}) immobilized onto a GCE at six different loadings. The electrodes were prepared by dropping the indicated volume of a freshly reduced 2.0 µM Cu DEN solution onto a GCE and drying under blowing N_2. The scans were collected in 0.10 M $HClO_4$ at a scan rate of 5.0 mV/s. (b) Dependence of i_p on the Cu loading.

A linear dependence of the peak current, i_p, to the Cu loading is also observed (Figure 5.11b). The behavior of i_p indicates that all of the deposited DENs are in electrical contact with the GCE. If the surface layers of the DENs were not in electrical contact, a constant i_p at high loading levels would be expected. This indicates that the difference in current between drop-cast free, reduced Cu salt and Cu DENs (Figures 5.1 and 5.4, respectively) is probably due to dissolution of the dendrimer film.

Size dependence. Figure 5.12 plots the anodic stripping waves of G6-OH(Cu_n) (n = 16, 32, 48,and 55).

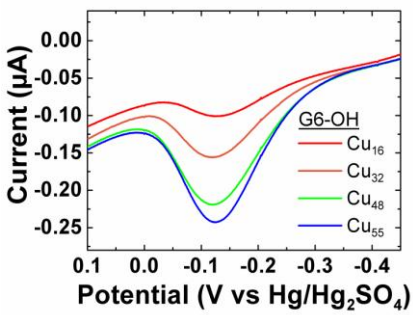

Figure 5.12.

Anodic stripping waves of G6-OH(Cu_x) (x = 16, 32, 48, 55) immobilized onto a GCE. The electrodes were prepared by dropping 0.50 µL of 2.0 µM Cu DEN solutions onto a GCE and drying in air and under blowing N_2. The scans were collected in 0.1 M $HClO_4$ at a scan rate of 10.0 mV/s.

No size-dependent shifts of E_p are observed and i_p is found to vary with the amount of Cu in the DEN. Assuming a quasi-spherical, fcc structure, Cu DENs in this size regime

have diameters ranging from 0.8-1.4 nm (G6-OH(Cu_{16}) and G6-OH(Cu_{55}), respectively).

In order to study the behavior of larger Cu particles, ASV of Cu DSNs was also performed (Figure 5.13).

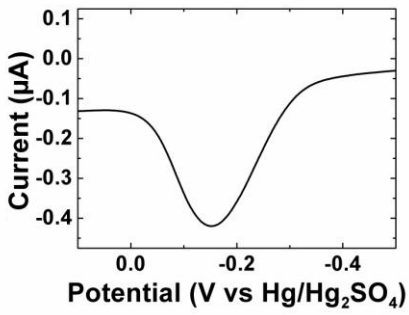

Figure 5.13.

Cu stripping wave of G6-OH(Cu_{310}) immobilized onto a GCE. The electrode was prepared by dropping 1.00 μL of a 2.0 μM Cu DSN solution onto a GCE and drying under blowing N_2. The scans were collected in 0.1 M $HClO_4$ at a scan rate of 5.0 mV/s.

It can be seen that no shifting of the peak position is observed, even for larger Cu nanoparticle structures. This indicates that the positive shift of DENs and DSNs relative to the free, reduced Cu salt is most likely caused by interaction of the Cu with the functional groups of the PAMAM dendrimer and not an effect of the nanoparticle size. It is interesting that when metal-ion-dendrimer complex is electrochemically reduced, no shift of the Cu stripping wave relative to the free, reduced Cu salt is observed. This indicates that intimate contact between the dendrimer and

the Cu metal is required to produce the positive shift in the anodic stripping wave.

5.4 Summary and Conclusions

Previous studies have shown that small, supported Cu nanoparticles are resistant to electrochemical oxidation.[133] Here it is demonstrated that very small Cu nanoparticles (~16 atoms) in the interior of a PAMAM dendrimer do not show this effect. A large, positive shift of the anodic stripping wave of Cu DENs and DSNs is observed. However, this positive shift requires intimate contact between the particle and the PAMAM dendrimer. Evidence for this comes from the similarity of E_p between reduced, free Cu salt and the electrochemically reduced metal-ion-dendrimer complex.

References

1. Zhao, M.; Sun, L.; Crooks, R. M. Preparation of Cu Nanoclusters within Dendrimer Templates. *J. Am. Chem. Soc.* 1998, *120*, 4877-4878.

2. Tarazona-Vasquez, F.; Balbuena, P. B. Pt(II) Uptake by Dendrimer Outer Pockets: 1. Solventless Ligand Exchange Reaction. *J. Phys. Chem. B* 2008, *112*, 4172-4181.

3. Tarazona-Vasquez, F.; Balbuena, P. B. Pt(II) Uptake by Dendrimer Outer Pockets: 2. Solvent-Mediated Complexation. *J. Phys. Chem. B* 2008, *112*, 4182-4193.

4. Sun, L.; Crooks, R. M. Interactions between Dendrimers and Charged Probe Molecules. 1. Theoretical Methods for Simulating Proton and Metal Ion Binding to Symmetric Polydentate Ligands. *J. Phys. Chem. B* 2002, *106*, 5864-5872.

5. Tarazona-Vasquez, F.; Balbuena, P. B. Complexation of Cu(II) Ions with the Lowest Generation Poly(amido-amine)-OH Dendrimers: A Molecular Simulation Study. *J. Phys. Chem. B* 2005, *109*, 12480-12490.

6. Krot, K. A.; Danil de Namor, A. F.; Aguilar-Cornejo, A.; Nolan, K. B. Speciation, stability constants and structures of complexes of copper(II), nickel(II), silver(I) and mercury(II) with PAMAM dendrimer and related tetraamide ligands. *Inorg. Chim. Acta* 2005, *358*, 3497-3505.

7. Tran, M. L.; Gahan, L. R.; Gentle, I. R. Structural Studies of Copper(II)-Amine Terminated Dendrimer Complexes by EXAFS. *J. Phys. Chem. B* 2004, *108*, 20130-20136.

8. Alexeev, O. S.; Siani, A.; Lafaye, G.; Williams, C. T.; Ploehn, H. J.; Amiridis, M. D. EXAFS Characterization of Dendrimer-Pt Nanocomposites Used for the Preparation of Pt/Al_2O_3 Catalysts. *J. Phys. Chem. B* 2006, *110*, 24903-24914.

9. Diallo, M. S.; Christie, S.; Swaminathan, P.; Balogh, L.; Shi, X.; Um, W.; Papelis, C.; Goddard, W. A., III; Johnson, J. H., Jr. Dendritic Chelating Agents. 1. Cu(II) Binding to Ethylene Diamine Core Poly(amidoamine) Dendrimers in Aqueous Solutions. *Langmuir* **2004**, *20*, 2640-2651.

10. Scott, R. W. J.; Datye, A. K.; Crooks, R. M. Bimetallic Palladium-Platinum Dendrimer-Encapsulated Catalysts. *J. Am. Chem. Soc.* **2003**, *125*, 3708-3709.

11. Ye, H.; Crooks, R. M. Effect of Elemental Composition of PtPd Bimetallic Nanoparticles Containing an Average of 180 Atoms on the Kinetics of the Electrochemical Oxygen Reduction Reaction. *J. Am. Chem. Soc.* **2007**, *129*, 3627-3633.

12. Weir, M. G.; Knecht, M. R.; Frenkel, A. I.; Crooks, R. M. Structural Analysis of PdAu Dendrimer-Encapsulated Bimetallic Nanoparticles. *Langmuir* **2010**, *26*, 1137-1146.

13. Gröhn, F.; Bauer, B. J.; Akpalu, Y. A.; Jackson, C. L.; Amis, E. J. Dendrimer Templates for the Formation of Gold Nanoclusters. *Macromolecules* **2000**, *33*, 6042-6050.

14. Scott, R. W. J.; Wilson, O. M.; Crooks, R. M. Synthesis, Characterization, and Applications of Dendrimer-Encapsulated Nanoparticles. *J. Phys. Chem. B* **2005**, *109*, 692-704.

15. Vohs, J. K.; Fahlman, B. D. Advances in the controlled growth of nanoclusters using a dendritic architecture. *New Journal of Chemistry* **2007**, *31*, 1041-1051.

16. Peng, X. H.; Pan, Q. M.; Rempel, G. L. Bimetallic dendrimer-encapsulated nanoparticles as catalysts: a review of the research advances. *Chem. Soc. Rev.* **2008**, *37*, 1619-1628.

17. Chandler, B. D.; Gilbertson, J. D. Dendrimer-Encapsulated Bimetallic Nanoparticles: Synthesis, Characterization, and Applications to Homogeneous and

Heterogeneous Catalysis. *Top. Organomet. Chem.* 2006, *20*, 97-120.

18. Aikens, C. M. Electronic Structure of Ligand-Passivated Gold and Silver Nanoclusters. *J. Phys. Chem. Lett.* 2011, *2*, 99-104.

19. Cuenya, B. R. Synthesis and catalytic properties of metal nanoparticles: Size, shape, support, composition, and oxidation state effects. *Thin Solid Films* 2010, *518*, 3127-3150.

20. Gomez, M. V.; Guerra, J.; Velders, A. H.; Crooks, R. M. NMR Characterization of Fourth-Generation PAMAM Dendrimers in the Presence and Absence of Palladium Dendrimer-Encapsulated Nanoparticles. *J. Am. Chem. Soc.* 2009, *131*, 341-350. Correction: *J. Am. Chem. Soc.* 2009, *131*, 15564.

21. Petkov, V.; Bedford, N.; Knecht, M. R.; Weir, M. G.; Crooks, R. M.; Tang, W.; Henkelman, G.; Frenkel, A. Periodicity and Atomic Ordering in Nanosized Particles of Crystals. *J. Phys. Chem. C* 2008, *112*, 8907-8911.

22. Somorjai, G. A.; Aliaga, C. Molecular Studies of Model Surfaces of Metals from Single Crystals to Nanoparticles under Catalytic Reaction Conditions. Evolution from Prenatal and Postmortem Studies of Catalysts. *Langmuir* 2010, *26*, 16190-16203.

23. Burda, C.; Chen, X.; Narayanan, R.; El-Sayed, M. A. Chemistry and Properties of Nanocrystals of Different Shapes. *Chem. Rev.* 2005, *105*, 1025-1102.

24. Lee, H.; Habas, S. E.; Kweskin, S.; Butcher, D.; Somorjai, G. A.; Yang, P. Morphological Control of Catalytically Active Platinum Nanocrystals. *Angew. Chem. Int. Ed.* 2006, *45*, 7824-7828.

25. Vögtle, F.; Richardt, G.; Werner, N. *Dendrimer Chemistry: Concepts, Syntheses, Properties, Applications*. Wiley-VCH: Weinheim, 2009.

26. Méry, D.; Astruc, D. Dendritic catalysis: Major concepts and recent progress. *Coord. Chem. Rev.* 2006, *250*, 1965-1979.

27. Cho, M. J.; Choi, D. H.; Sullivan, P. A.; Akelaitis, A. J. P.; Dalton, L. R. Recent progress in second-order nonlinear optical polymers and dendrimers. *Progress in Polymer Science* 2008, *33*, 1013-1058.

28. Astruc, D.; Ornelas, C.; Ruiz, J. Metallocenyl Dendrimers and Their Applications in Molecular Electronics, Sensing, and Catalysis. *Acc. Chem. Res.* 2008, *41*, 841-856.

29. Li, W.-S.; Aida, T. Dendrimer Porphyrins and Phthalocyanines. *Chem. Rev.* 2009, *109*, 6047-6076.

30. Astruc, D.; Boisselier, E.; Ornelas, C. Dendrimers Designed for Functions: From Physical, Photophysical, and Supramolecular Properties to Applications in Sensing, Catalysis, Molecular Electronics, Photonics, and Nanomedicine. *Chem. Rev.* 2010, *110*, 1857-1959.

31. Liu, Y.; Bryantsev, V. S.; Diallo, M. S.; Goddard, W. A., III PAMAM Dendrimers Undergo pH Responsive Conformational Changes without Swelling. *J. Am. Chem. Soc.* 2009, *131*, 2798-2799.

32. Li, T.; Hong, K.; Porcar, L.; Verduzco, R.; Butler, P. D.; Smith, G. S.; Liu, Y.; Chen, W.-R. Assess the Intramolecular Cavity of a PAMAM Dendrimer in Aqueous Solution by Small-Angle Neutron Scattering. *Macromolecules* 2008, *41*, 8916-8920.

33. Chen, W.-R.; Porcar, L.; Liu, Y.; Butler, P. D.; Magid, L. J. Small Angle Neutron Scattering Studies of the Counterion Effects on the Molecular Conformation and Structure of Charged G4 PAMAM Dendrimers in Aqueous Solutions. *Macromolecules* 2007, *40*, 5887-5898.

34. Li, X.; Zamponi, M.; Hong, K.; Porcar, L.; Shew, C.-Y.; Jenkins, T.; Liu, E.; Smith, G. S.; Herwig, K. W.; Liu, Y.; Chen, W.-R. pH Responsiveness of polyelectrolyte

dendrimers: a dynamical perspective. *Soft Matter* 2011, *7*, 618-622.

35. Niu, Y.; Crooks, R. M. Preparation of Dendrimer-Encapsulated Metal Nanoparticles Using Organic Solvents. *Chem. Mater.* 2003, *15*, 3463-3467.

36. Yeung, L. K.; Crooks, R. M. Heck Heterocoupling within a Dendritic Nanoreactor. *Nano Lett.* 2001, *1*, 14-17.

37. Satoh, N.; Nakashima, T.; Kamikura, K.; Yamamoto, K. Quantum size effect in TiO_2 nanoparticles prepared by finely controlled metal assembly on dendrimer templates. *Nat. Nanotechnol.* 2008, *3*, 106-111.

38. Nakamula, I.; Yamanoi, Y.; Yonezawa, T.; Imaoka, T.; Yamamoto, K.; Nishihara, H. Nanocage catalysts-rhodium nanoclusters encapsulated with dendrimers as accessible and stable catalysts for olefin and nitroarene hydrogenations. *Chem. Commun.* 2008, 5716-5718.

39. Ornelas, C.; Aranzaes, J. R.; Salmon, L.; Astruc, D. “Click” Dendrimers: Synthesis, Redox Sensing of Pd(OAc)2, and Remarkable Catalytic Hydrogenation Activity of Precise Pd Nanoparticles Stabilized by 1,2,3-Triazole-Containing Dendrimers. *Chem. Eur. J.* 2008, *14*, 50-64.

40. Ornelas, C.; Salmon, L.; Aranzaes, J. R.; Astruc, D. Catalytically efficient palladium nanoparticles stabilized by "click" ferrocenyl dendrimers. *Chem. Commun.* 2007, 4946-4948.

41. Diallo, A. K.; Ornelas, C.; Salmon, L.; Aranzaes, J. R.; Astruc, D. "Homeopathic" catalytic activity and atom-leaching mechanism in Miyaura-Suzuki reactions under ambient conditions with precise dendrimer-stabilized Pd nanoparticles. *Angew. Chem. Int. Ed.* 2007, *46*, 8644-8648.

42. Knecht, M. R.; Garcia-Martinez, J. C.; Crooks, R. M. Synthesis, Characterization, and Magnetic Properties of

Dendrimer-Encapsulated Nickel Nanoparticles Containing <150 Atoms. *Chem. Mater.* 2006, *18*, 5039-5044.

43. Gates, A. T.; Nettleton, E. G.; Myers, V. S.; Crooks, R. M. Synthesis and Characterization of NiSn Dendrimer-Encapsulated Nanoparticles. *Langmuir* 2010, *26*, 12994-12999.

44. Knecht, M. R.; Crooks, R. M. Magnetic properties of dendrimer-encapsulated iron nanoparticles containing an average of 55 and 147 atoms. *New J. Chem.* 2007, *31*, 1349-1353.

45. Knecht, M. R.; Weir, M. G.; Myers, V. S.; Pyrz, W. D.; Ye, H.; Petkov, V.; Buttrey, D. J.; Frenkel, A. I.; Crooks, R. M. Synthesis and Characterization of Pt Dendrimer-Encapsulated Nanoparticles: Effect of the Template on Nanoparticle Formation. *Chem. Mater.* 2008, *20*, 5218-5228.

46. Zhao, M.; Crooks, R. M. Intradendrimer Exchange of Metal Nanoparticles. *Chem. Mater.* 1999, *11*, 3379-3385.

47. Zhang, J.; Mo, Y.; Vukmirovic, M. B.; Klie, R.; Sasaki, K.; Adzic, R. R. Platinum Monolayer Electrocatalysts for O_2 Reduction: Pt Monolayer on Pd(111) and on Carbon-Supported Pd Nanoparticles. *J. Phys. Chem. B* 2004, *108*, 10955-10964.

48. Pande, S.; Weir, M. G.; Zaccheo, B. A.; Crooks, R. M. Synthesis, characterization, and electrocatalysis using Pt and Pd dendrimer-encapsulated nanoparticles prepared by galvanic exchange. *New J. Chem.* 2011, *35*, 2054-2060.

49. Bard, A. J.; Faulkner, L. R. *Electrochemical Methods Fundamentals and Application*; 2nd ed. John Wiley & Sons: New York, 2001.

50. Knecht, M. R.; Weir, M. G.; Frenkel, A. I.; Crooks, R. M. Structural Rearrangement of Bimetallic Alloy PdAu Nanoparticles within Dendrimer Templates to Yield

Core/Shell Configurations. *Chem. Mater.* 2008, *20*, 1019-1028.

51. Myers, S. V.; Frenkel, A. I.; Crooks, R. M. X-ray Absorption Study of PdCu Bimetallic Alloy Nanoparticles Containing an Average of ~64 Atoms. *Chem. Mater.* 2009, *21*, 4824-4829.

52. Carino, E. V.; Crooks, R. M. Characterization of Pt@Cu Core@Shell Dendrimer-Encapsulated Nanoparticles Synthesized by Cu Underpotential Deposition. *Langmuir* 2011, *27*, 4227-4235.

53. Yancey, D. F.; Carino, E. V.; Crooks, R. M. Electrochemical Synthesis and Electrocatalytic Properties of Au@Pt Dendrimer-Encapsulated Nanoparticles. *J. Am. Chem. Soc.* 2010, *132*, 10988-10989.

54. Lang, H.; Maldonado, S.; Stevenson, K. J.; Chandler, B. D. Synthesis and Characterization of Dendrimer Templated Supported Bimetallic Pt@Au Nanoparticles. *J. Am. Chem. Soc.* 2004, *126*, 12949-12956.

55. Frenkel, A. I. Solving the 3D structure of metal nanoparticles. *Z. Krystallogr.* 2007, *222*, 605-611.

56. Ozturk, O.; Black, T. J.; Perrine, K.; Pizzolato, K.; Williams, C. T.; Parsons, F. W.; Ratliff, J. S.; Gao, J.; Murphy, C. J.; Xie, H.; Ploehn, H. J.; Chen, D. A. Thermal Decomposition of Generation-4 Polyamidoamine Dendrimer Films: Decomposition Catalyzed by Dendrimer-Encapsulated Pt Particles. *Langmuir* 2005, *21*, 3998-4006.

57. Ye, H.; Crooks, R. M. Electrocatalytic O_2 Reduction at Glassy Carbon Electrodes Modified with Dendrimer-Encapsulated Pt Nanoparticles. *J. Am. Chem. Soc.* 2005, *127*, 4930-4934.

58. Zhao, M.; Crooks, R. M. Dendrimer-Encapsulated Pt Nanoparticles. Synthesis, Characterization, and

Applications to Catalysis. *Adv. Mater.* 1999, *11*, 217-220.

59. Gu, Y.; Sanders, P.; Ploehn, H. J. Quantitative analysis of Pt-PAMAM ligand exchange reactions: Time and concentration effects. *Colloids Surf., A* 2010, *356*, 10-15.

60. Gu, Y.; Xie, H.; Gao, J.; Liu, D.; Williams, C. T.; Murphy, C. J.; Ploehn, H. J. AFM Characterization of Dendrimer-Stabilized Platinum Nanoparticles. *Langmuir* 2005, *21*, 3122-3131.

61. Wilson, O. M.; Scott, R. W. J.; Garcia-Martinez, J. C.; Crooks, R. M. Synthesis, Characterization and Structure-Selective Extraction of AuAg Bimetallic Nanoparticles. *J. Am. Chem. Soc.* 2005, 1015-1024.

62. Gomez, M. V.; Guerra, J.; Myers, V. S.; Crooks, R. M.; Velders, A. H. Nanoparticle Size Determination by 1H NMR Spectroscopy. *J. Am. Chem. Soc.* 2009, *131*, 14634-14635.

63. Parker, J. F.; Fields-Zinna, C. A.; Murray, R. W. The Story of a Monodisperse Gold Nanoparticle: $Au_{25}L_{18}$. *Acc. Chem. Res.* 2010, *43*, 1289-1296.

64. Müller, R.; Laschober, C.; Szymanski, W. W.; Allmaier, G. Determination of Molecular Weight, Particle Size, and Density of High Number Generation PAMAM Dendrimers Using MALDI-TOF-MS and nES-GEMMA. *Macromolecules* 2007, *40*, 5599-5605.

65. Albiter, M. A.; Crooks, R. M.; Zaera, F. Adsorption of Carbon Monoxide on Dendrimer-Encapsulated Platinum Nanoparticles: Liquid versus Gas Phase. *J. Phys. Chem. Lett.* 2010, *1*, 38-40.

66. Wales, C. H.; Berger, J.; Blass, S.; Crooks, R. M.; Asherie, N. Quasi-Elastic Light Scattering of Platinum Dendrimer-Encapsulated Nanoparticles. *Langmuir* 2011, *27*, 4104-4109.

67. Ye, H.; Crooks, J. A.; Crooks, R. M. Effect of Particle Size on the Kinetics of the Electrocatalytic Oxygen Reduction Reaction Catalyzed by Pt Dendrimer-Encapsulated Nanoparticles. *Langmuir* 2007, *23*, 11901-11906.

68. Zhao, M.; Tokuhisa, H.; Crooks, R. M. Molecule-Sized Gates Based on Surface-Confined Dendrimers. *Angew. Chem. Int. Ed. Engl.* 1997, *36*, 2596-2598.

69. Kim, T. H.; Choi, H. S.; Go, B. R.; Kim, J. Modification of a glassy carbon surface with amine-terminated dendrimers and its application to electrocatalytic hydrazine oxidation. *Electrochem. Commun.* 2010, *12*, 788-791.

70. Vijayaraghavan, G.; Stevenson, K. J. Synergistic Assembly of Dendrimer-Templated Platinum Catalysts on Nitrogen-Doped Carbon Nanotube Electrodes for Oxygen Reduction. *Langmuir* 2007, *23*, 5279-5282.

71. Shen, Y.; Xu, Q.; Gao, H.; Zhu, N. Dendrimer-encapsulated Pd nanoparticles anchored on carbon nanotubes for electro-catalytic hydrazine oxidation. *Electrochem. Commun.* 2009, *11*, 1329-1332.

72. Herrero, E.; Buller, L. J.; Abruña, H. D. Underpotential Deposition at Single Crystal Surfaces of Au, Pt, Ag and Other Materials. *Chem. Rev.* 2001, *101*, 1897-1930.

73. Zhang, J.; Lima, F. H. B.; Shao, M. H.; Sasaki, K.; Wang, J. X.; Hanson, J.; Adzic, R. R. Platinum Monolayer on Nonnoble Metal-Noble Metal Core-Shell Nanoparticle Electrocatalysts for O_2 Reduction. *J. Phys. Chem. B* 2005, *109*, 22701-22704.

74. Wang, J. X.; Inada, H.; Wu, L.; Zhu, Y.; Choi, Y.; Liu, P.; Zhou, W.-P.; Adzic, R. R. Oxygen Reduction on Well-Defined Core-Shell Nanocatalysts: Particle Size, Facet, and Pt Shell Thickness Effects. *J. Am. Chem. Soc.* 2009, *131*, 17298-17302.

75. Zhai, J.; Huang, M.; Dong, S. Electrochemical Designing of Au/Pt Core Shell Nanoparticles as Nanostructured Catalyst with Tunable Activity for Oxygen Reduction. *Electroanal.* **2007**, *19*, 506-509.

76. Li, X.; Liu, J.; He, W.; Huang, Q.; Yang, H. Influence of the composition of core-shell Au-Pt nanoparticle electrocatalysts for the oxygen reduction reaction. *J. Colloid Interface Sci.* **2010**, *344*, 132-136.

77. Gong, K.; Su, D.; Adzic, R. R. Platinum-Monolayer Shell on $AuNi_{0.5}Fe$ Nanoparticle Core Electrocatalyst with High Activity and Stability for the Oxygen Reduction Reaction. *J. Am. Chem. Soc.* **2010**, *132*, 14364-14366.

78. Biegler, T.; Rand, D. A. J.; Woods, R. Limiting oxygen coverage on platinized platinum; Relevance to determination of real platinum area by hydrogen adsorption. *J. Electroanal. Chem.* **1971**, *29*, 269-277.

79. Fernandez, J. L.; White, J. M.; Sun, Y. M.; Tang, W. J.; Henkelman, G.; Bard, A. J. Characterization and theory of electrocatalysts based on scanning electrochemical microscopy screening methods. *Langmuir* **2006**, *22*, 10426-10431.

80. Greeley, J.; Nørskov, J. K. A general scheme for the estimation of oxygen binding energies on binary transition metal surface alloys. *Surf. Sci.* **2005**, *592*, 104-111.

81. Nilekar, A. U.; Xu, Y.; Zhang, J. L.; Vukmirovic, M. B.; Sasaki, K.; Adzic, R. R.; Mavrikakis, M. Bimetallic and ternary alloys for improved oxygen reduction catalysis. *Top. Catal.* **2007**, *46*, 276-284.

82. Tang, W.; Henkelman, G. Charge redistribution in core-shell nanoparticles to promote oxygen reduction. *J. Chem. Phys.* **2009**, *130*, 194504.

83. Bian, C. R.; Suzuki, S.; Asakura, K.; Ping, L.; Toshima, N. Extended X-ray Absorption Fine Structure Studies on the Structure of the Poly(vinylpyrrolidone)-

Stabilized Cu/Pd Nanoclusters Colloidally Dispersed in Solution. *J. Phys. Chem. B* 2002, *106*, 8587-8598.

84. Molenbroek, A. M.; Haukka, S.; Clausen, B. S. Alloying in Cu/Pd Nanoparticle Catalysts. *J. Phys. Chem. B* 1998, *102*, 10680-10689.

85. Myers, V. S.; Weir, M. G.; Carino, E. V.; Yancey, D. F.; Pande, S.; Crooks, R. M. Dendrimer-encapsulated nanoparticles: New synthetic and characterization methods and catalytic applications. *Chem. Sci.* 2011, *2*, 1632 - 1646.

86. Scott, R. W. J.; Ye, H.; Henriquez, R. R.; Crooks, R. M. Synthesis, Characterization, and Stability of Dendrimer-Encapsulated Palladium Nanoparticles. *Chem. Mater.* 2003, *15*, 3873-3878.

87. Ravel, B.; Newville, M. ATHENA, ARTEMIS, HEPHAESTUS: Data Analysis for X-ray Absorption Spectroscopy using IFEFFIT. *J. Synchroton Rad.* 2005, *12*, 537-541.

88. Zabinsky, S. I.; Rehr, J. J.; Ankudinov, A.; Albers, R. C.; Eller, M. J. Multiple-scattering calculations of x-ray-absorption spectra. *Phys. Rev. B: Condens. Matter* 1995, *52*, 2995.

89. Wan, H.; Li, S.; Konovalova, T. A.; Shuler, S. F.; Dixon, D. A.; Street, S. C. Experimental and Theoretical Studies of the Photoreduction of Copper(II)-Dendrimer Complexes. *J. Phys. Chem. C* 2008, *112*, 1335-1344.

90. Creighton, J. A.; Eadon, D. G. Ultraviolet-visible Absorption Spectra of the Colloidal Metallic Elements. *J. Chem. Soc., Faraday Trans.* 1991, *87*, 3881-3891.

91. Pileni, M. P.; Lisiecki, I. Nanometer metallic copper particle synthesis in reverse micelles. *Colloids Surf., A* 1993, *80*, 63-68.

92. Carino, E. V.; Knecht, M. R.; Crooks, R. M. Quantitative Analysis of the Stability of Pd Dendrimer-Encapsulated Nanoparticles. *Langmuir* 2009, *25*, 10279-10284.

93. Via, G. H.; Drake, K. F.; Meitzner, G.; Lytle, F. W.; Sinfelt, J. H. Analysis of EXAFS data on bimetallic clusters. *Catal. Lett.* 1990, *5*, 25-33.

94. Montejano-Carrizales, J. M.; Aguilera-Granja, F.; Morán-López, J. L. Direct Enumeration of the Geometrical Characteristics of Clusters. *Nanostruct. Mater.* 1997, *8*, 269-287.

95. Frenkel, A. I. Solving the structure of nanoparticles by multiple-scattering EXAFS analysis. *J. Synchrotron Radiat.* 1999, *6*, 293-295.

96. Frenkel, A. I.; Hills, C. W.; Nuzzo, R. G. A View from the Inside: Complexity in the Atomic Scale Ordering of Supported Metal Nanoparticles. *J. Phys. Chem. B* 2001, *105*, 12689-12703.

97. Tew, M. W.; Miller, J. T.; van Bokhoven, J. A. Particle Size Effect of Hydride Formation and Surface Hydrogen Adsorption of Nanosized Palladium Catalysts: L3 Edge vs K Edge X-ray Absorption Spectroscopy. *J. Phys. Chem. BC* 2009, *113*, 15140-15147.

98. Tang, W.; Zhang, L.; Henkelman, G. Catalytic Activity of Pd/Cu Random Alloy Nanoparticles for Oxygen Reduction. *J. Phys. Chem. Lett.* 2011, *2*, 1328-1331.

99. Niu, Y.; Yeung, L. K.; Crooks, R. M. Size-Selective Hydrogenation of Olefins by Dendrimer-Encapsulated Palladium Nanoparticles. *J. Am. Chem. Soc.* 2001, *123*, 6840-6846.

100. Weir, M. G.; Myers, V. S.; Frenkel, A. I.; Crooks, R. M. In situ X-ray Absorption Analysis of ~1.8 nm Dendrimer-Encapsulated Pt Nanoparticles during Electrochemical CO Oxidation. *ChemPhysChem* 2010, *11*, 2942-2950.

101. Arruda, T. M.; Shyam, B.; Ziegelbauer, J. M.; Mukerjee, S.; Ramaker, D. E. Investigation into the Competitive and Site-Specific Nature of Anion Adsorption on Pt Using In Situ X-ray Absorption Spectroscopy. *J. Phys. Chem. C* 2008, *112*, 18087-18097.

102. Mukerjee, S.; McBreen, J. Effect of particle size on the electrocatalysis by carbon-supported Pt electrocatalysts: an in situ XAS investigation. *J. Electroanal. Chem.* 1998, *448*, 163-171.

103. Mukerjee, S.; Srinivasan, S.; Soriaga, M. P.; McBreen, J. Effect of Preparation Conditions of Pt Alloys on Their Electronic, Structural, and Electrocatalytic Activities for Oxygen Reduction - XRD, XAS, and Electrochemical Studies. *J. Phys. Chem.* 1995, *99*, 4577-4589.

104. Sanjeev, M.; Supramaniam, S.; Manuel, P. S.; James, M. Role of Structural and Electronic Properties of Pt and Pt Alloys on Electrocatalysis of Oxygen Reduction. *J. Electrochem. Soc.* 1995, *142*, 1409-1422.

105. Maniguet, S.; Mathew, R. J.; Russell, A. E. EXAFS of Carbon Monoxide Oxidation on Supported Pt Fuel Cell Electrocatalysts. *J. Phys. Chem. B* 2000, *104*, 1998-2004.

106. Lampitt, R. A.; Carrette, L. P. L.; Hogarth, M. P.; Russell, A. E. In situ and model EXAFS studies of electrocatalysts for methanol oxidation. *J. Electroanal. Chem.* 1999, *460*, 80-87.

107. Russell, A. E.; Maniguet, S.; Mathew, R. J.; Yao, J.; Roberts, M. A.; Thompsett, D. In situ X-ray absorption spectroscopy and X-ray diffraction of fuel cell electrocatalysts. *J. Power Sources* 2001, *96*, 226-232.

108. Teliska, M.; O'Grady, W. E.; Ramaker, D. E. Determination of O and OH Adsorption Sites and Coverage in Situ on Pt Electrodes from Pt L_{23} X-ray Absorption Spectroscopy. *J. Phys. Chem. B* 2005, *109*, 8076-8084.

109. Murthi, V. S.; Urian, R. C.; Mukerjee, S. Oxygen Reduction Kinetics in Low and Medium Temperature Acid Environment: Correlation of Water Activation and Surface Properties in Supported Pt and Pt Alloy Electrocatalysts. *J. Phys. Chem. B* **2004**, *108*, 11011-11023.

110. Imai, H.; Izumi, K.; Matsumoto, M.; Kubo, Y.; Kato, K.; Imai, Y. In Situ and Real-Time Monitoring of Oxide Growth in a Few Monolayers at Surfaces of Platinum Nanoparticles in Aqueous Media. *J. Am. Chem. Soc.* **2009**, *131*, 6293-6300.

111. Mathew, R. J.; Russell, A. E. XAS of carbon supported platinum fuel cell electrocatalysts: advances towards real time investigations. *Top. Catal.* **2000**, *10*, 231-239.

112. Antolini, E.; Salgado, J. R. C.; Giz, M. J.; Gonzalez, E. R. Effects of geometric and electronic factors on ORR activity of carbon supported Pt-Co electrocatalysts in PEM fuel cells. *Int. J. Hydrogen Energy* **2005**, *30*, 1213-1220.

113. Russell, A. E.; Rose, A. X-ray Absorption Spectroscopy of Low Temperature Fuel Cell Catalysts. *Chem. Rev.* **2004**, *104*, 4613-4636.

114. Tada, M.; Murata, S.; Asakoka, T.; Hiroshima, K.; Okumura, K.; Tanida, H.; Uruga, T.; Nakanishi, H.; Matsumoto, S.-i.; Inada, Y.; Nomura, M.; Iwasawa, Y. In Situ Time-Resolved Dynamic Surface Events on the Pt/C Cathode in a Fuel Cell under Operando Conditions. *Angew. Chem.* **2007**, *119*, 4388-4393.

115. Hudson, S. L.; Balla, S. C.; Blaney, K. B.; Chouchelamaneb, G. H.; Fiddy, S. G.; Harvey, I.; Sivasubramaniamb, P.; Tessiera, B. C.; Theobalda, B. R. C.; Thompsetta, D.; Russell, A. E. Probing The Structure Of Operating Fuel Cell Cathode Catalysts Using XAS. *ECS Transactions* **2008**, *16*, 1395-1404.

116. Principi, E.; Witkowska, A.; Dsoke, S.; Marassi, R.; Di Cicco, A. An XAS experimental approach to study low Pt

content electrocatalysts operating in PEM fuel cells. *Phys. Chem. Chem. Phys.* 2009, *11*, 9987-9995.

117. Witkowska, A.; Principi, E.; Di Cicco, A.; Dsoke, S.; Marassi, R.; Olivi, L.; Centazzo, M.; Albertini, V. R. Temperature and potential-dependent structural changes in a Pt cathode electrocatalyst viewed by in situ XAFS. *J. Non-Cryst. Solids* 2008, *354*, 4227-4232.

118. Ledesma-García, J.; Escalante García, I. L.; Rodríguez, F. J.; Chapman, T. W.; Godínez, L. A. Immobilization of dendrimer-encapsulated platinum nanoparticles on pretreated carbon-fiber surfaces and their application for oxygen reduction. *J. Appl. Electrochem.* 2008, *38*, 515-522.

119. Glasner, D.; Frenkel, A. I. Geometrical Characteristics of Regular Polyhedra: Application to EXAFS Studies of Nanoclusters. *XAFS13 Conference Proceedings* 2007, *882*, 746-748.

120. Roldan Cuenya, B.; Frenkel, A. I.; Mostafa, S.; Behafarid, F.; Croy, J. R.; Ono, L. K.; Wang, Q. Anomalous lattice dynamics and thermal properties of supported size- and shape-selected Pt nanoparticles. *Phys. Rev. B* 2010, *82*, 155450.

121. Roldan Cuenya, B.; Croy, J. R.; Mostafa, S.; Behafarid, F.; Li, L.; Zhang, Z.; Yang, J. C.; Wang, Q.; Frenkel, A. I. Solving the Structure of Size-Selected Pt Nanocatalysts Synthesized by Inverse Micelle Encapsulation. *J. Am. Chem. Soc.* 2010, *132*, 8747-8756.

122. Menard, L. D.; Xu, H.; Gao, S.-P.; Twesten, R. D.; Harper, A. S.; Song, Y.; Wang, G.; Douglas, A. D.; Yang, J. C.; Frenkel, A. I.; Murray, R. W.; Nuzzo, R. G. Metal Core Bonding Motifs of Monodisperse Icosahedral Au13 and Larger Au Monolayer-Protected Clusters As Revealed by X-ray Absorption Spectroscopy and Transmission Electron Microscopy. *J. Phys. Chem. B* 2006, *110*, 14564-14573.

123. Guliamov, O.; Frenkel, A. I.; Menard, L. D.; Nuzzo, R. G.; Kronik, L. Tangential Ligand-Induced Strain in

Icosahedral Au13. *J. Am. Chem. Soc.* 2007, *129*, 10978-10979.

124. Yevick, A.; Frenkel, A. I. Effects of surface disorder on EXAFS modeling of metallic clusters. *Phys. Rev. B* 2010, *81*, 115451.

125. Frenkel, A.; Stern, E. A.; Voronel, A.; Qian, M.; Newville, M. Buckled crystalline structure of mixed ionic salts. *Phys. Rev. Lett.* 1993, *71*, 3485-3488.

126. Frenkel, A.; Stern, E. A.; Voronel, A.; Qian, M.; Newville, M. Solving the structure of disordered mixed salts. *Phys. Rev. B* 1994, *49*, 11662-11674.

127. Wilson, O. M.; Knecht, M. R.; Garcia-Martinez, J. C.; Crooks, R. M. Effect of Pd Nanoparticle Size on the Catalytic Hydrogenation of Allyl Alcohol. *J. Am. Chem. Soc.* 2006, *128*, 4510-4511.

128. Plieth, W. J. Electrochemical properties of small clusters of metal atoms and their role in the surface enhanced Raman scattering. *J. Phys. Chem.* 1982, *86*, 3166-3170.

129. Tang, L.; Li, X.; Cammarata, R. C.; Friesen, C.; Sieradzki, K. Electrochemical Stability of Elemental Metal Nanoparticles. *J. Am. Chem. Soc.* 2010, *132*, 11722-11726.

130. Ivanova, O. S.; Zamborini, F. P. Size-Dependent Electrochemical Oxidation of Silver Nanoparticles. *J. Am. Chem. Soc.* 2010, *132*, 70-72.

131. Ivanova, O. S.; Zamborini, F. P. Electrochemical Size Discrimination of Gold Nanoparticles Attached to Glass/Indium-Tin-Oxide Electrodes by Oxidation in Bromide-Containing Electrolyte. *Anal. Chem.* 2010, *82*, 5844-5850.

132. Ng, K. H.; Liu, H.; Penner, R. M. Subnanometer Silver Clusters Exhibiting Unexpected Electrochemical

Metastability on Graphite. *Langmuir* 2000, *16*, 4016-4023.

133. Kolb, D. M.; Engelmann, G. E.; Ziegler, J. C. On the Unusual Electrochemical Stability of Nanofabricated Copper Clusters. *Angew. Chem. Int. Ed.* 2000, *39*, 1123-1125.

134. Berchmans, S.; Vergheese, T. M.; Kavitha, A. L.; Veerakumar, M.; Yegnaraman, V. Electrochemical preparation of copper-dendrimer nanocomposites: picomolar detection of Cu^{2+} ions. *Anal. Bioanal. Chem.* 2008, *390*, 939-946.

135. Ward Jones, S. E.; Campbell, F. W.; Baron, R.; Xiao, L.; Compton, R. G. Particle Size and Surface Coverage Effects in the Stripping Voltammetry of Silver Nanoparticles: Theory and Experiment. *J. Phys. Chem. C* 2008, *112*, 17820-17827.

Vita

Vera Sue Myers was born in New Orleans, Louisiana but spent most of her early years on the north shore of Lake Pontchartrain in Mandeville, Louisiana. She graduated *summa cum laude* with a double B.A. degree in chemistry and biochemistry from the University of Colorado at Boulder. She spent several years as a chemist at Boundless Corporation doing research on lithium ion battery technologies before pursuing her doctorate at the University of Texas.

Permanent email: vsuemyers@utexas.edu

This dissertation was typed by Vera Sue Myers.